Facultad de Ciencias

Búsqueda de los núcleos galácticos activos más oscurecidos con XMM-Newton y *Athena*.

(The search for the most obscured active galactic nuclei with XMM-Newton and *Athena*)

Trabajo de Fin de Máster
para acceder al

MÁSTER INTERUNIVERSITARIO EN FÍSICA DE PARTÍCULAS Y DEL COSMOS

Autor: Lorenzo Barquín González

Directores: Silvia Mateos Ibáñez
Francisco J. Carrera Troyano

Octubre - 2019

Agradecimientos

Agradecer primero a mis directores de trabajo de fin de máster, Silvia Mateos y Francisco Carrera; sin su ayuda y paciencia este trabajo no sería posible. También a mis compañeros, tanto de máster como del grupo de Galaxias y AGNs del IFCA, que me han ayudado a lo largo de todo el curso académico. Por último a mis padres, que siempre me han apoyado y animado a estudiar aquello que me apasiona.

Resumen

Una de las cuestiones más importantes de la astrofísica moderna es comprender como se han formado y han evolucionado las galaxias a lo largo de la historia del Universo. En las últimas décadas se han descubierto claras evidencias observacionales de que las galaxias crecen conjuntamente con el agujero negro supermasivo que la mayoría (quizás todas) presentan en su núcleo. Por tanto para avanzar en este campo es necesario comprender las propiedades de estos agujeros negros supermasivos. En particular de aquellos que se encuentran en una fase activa de crecimiento (aumento de su masa) acretando material de la galaxia huésped. Estos son los que se conocen como núcleos galácticos activos (por sus siglas en inglés AGN). De ellos, son de especial interés los AGNs altamente oscurecidos, pues se cree que en esta fase se establece la relación entre galaxia y agujero negro supermasivo. Este oscurecimiento es provocado por una estructura de gas y polvo denominada toro. Aquellos AGNs con oscurecimientos muy elevados – los denominados *Compton Thick* (CT) – se pierden en muestreos en las longitudes de onda ópticas y, en menor medida, en rayos X al estar absorbida la radiación emitida en estos rangos. Para detectar estos AGNs se suele recurrir al infrarrojo medio, donde el efecto del oscurecimiento es mucho menor. No obstante, su estudio en rayos X es fundamental para determinar el nivel de oscurecimiento.

Existen relaciones empíricas en la literatura que relacionan la luminosidad de los AGNs en el infrarrojo medio y en rayos X. El primer objetivo de este trabajo es comprobar si estas relaciones describen adecuadamente la relación entre luminosidades en muestras de AGNs seleccionados en el infrarrojo medio (como la utilizada en este trabajo) y, si no, encontrar una relación propia. El segundo objetivo de este trabajo es estimar un límite inferior del oscurecimiento para AGNs seleccionados en el infrarrojo medio pero no detectados en observaciones profundas en rayos X con el observatorio espacial XMM-*Newton*. Por último, en este trabajo se estima el tiempo necesario para la detección de este tipo de objetos con los observatorios de rayos X XMM-*Newton* y *Athena*.

Para cumplir estos objetivos científicos se dispone de una muestra seleccionada en el infrarrojo medio de 91 AGNs: 68 detectados en rayos X con XMM-*Newton*, 3 detectados pero con espectros de rayos X de baja calidad y 20 AGNs no detectados. Al ser una muestra seleccionada en el infrarrojo medio se espera que presente valores de oscurecimiento a lo largo del todo el espacio de parámetros. Se espera que los AGNs no detectados en rayos X o con espectros de baja calidad estén muy oscurecidos e incluso algunos de ellos sean CT. Estos (23) forman nuestra

muestra de candidatos a CT. Para los AGNs no detectados en rayos X tenemos un límite superior del flujo en rayos X y para aquellos con espectro de baja calidad tenemos medidas de la luminosidad observada, no corregida por el oscurecimiento. Estas medidas se usarán para determinar el nivel de oscurecimiento.

Primero se obtuvo la luminosidad intrínseca (corregida por el efecto del oscurecimiento) en rayos X para los AGNs candidatos a CT. Para ello se comprobó primero si las relaciones empíricas de la literatura entre las luminosidades en rayos X y en el infrarrojo medio son validas para muestras de AGNs seleccionadas en el infrarrojo medio. Dado que encontramos que todas ellas sobrestimaban la luminosidad en rayos X de los AGNs detectados en rayos X, fue necesario obtener una relación empírica propia. A partir de ella se obtuvo la luminosidad intrínseca en rayos X para los AGNs candidatos a CT asumiendo que siguen la misma relación que los detectados. A continuación se estimó el límite inferior del oscurecimiento de los AGNs candidatos a CT. Para ello se modeló su emisión en rayos X con un modelo de toro y se usaron las luminosidades intrínsecas en rayos X obtenidas para cada objeto a partir de su luminosidad infrarroja. Se realizaron simulaciones en las que al modelo de toro se le fue aumentando el oscurecimiento hasta alcanzar el límite superior en flujo o la luminosidad observada. Una vez conocido su oscurecimiento se estimó el tiempo que llevaría detectarlos con los observatorios de rayos X XMM-*Newton* y *Athena*. Para ello se realizaron nuevas simulaciones con el mismo modelo de toro imponiendo un cociente señal-ruido de 5 como criterio para aceptar la detección.

En este trabajo se ha encontrado que: a) los AGNs seleccionados en el infrarrojo medio son intrínsecamente débiles en rayos X frente a aquellos seleccionados en rayos X, por lo que las relaciones tradicionales sobrestiman su luminosidad intrínseca en rayos X; b) la absorción de los AGNs candidatos a CT es muy elevada e incluso extrema en la mayoría de los objetos; c) no es posible detectar los AGNs más oscurecidos de la muestra con la actual generación de observatorios de rayos X en un tiempo razonable; d) *Athena* será capaz de detectar la población de AGNs altamente oscurecidos de manera rutinaria en los muestreos extragalácticos planeados para la misión.

Palabras clave: rayos X, infrarrojo, núcleo galáctico activo, densidad columna, oscurecimiento en rayos X, XMM-*Newton*, *Athena*, detección, Compton thick

Abstract

One of the most important questions in modern astrophysics is the study of the formation and evolution of galaxies throughout the history of the Universe. In the last decades, several pieces of evidence have been found that support a co-evolution of galaxies with the supermassive black hole (SMBH) that most of them (maybe every galaxy) have in their centres. Consequently, to make progress in this field it is necessary to understand the properties of these SMBH. Particularly of those in an active phase of growing (increasing their mass) accreting material from the host galaxy. They are the so-called active galactic nuclei (AGN). Of these, the most highly obscured systems are of special interest, since it is believed that during this highly obscured phase the relationship between SMBHs and their hosts was established. The obscuration is caused by a dust and gas structure, the so-called torus. The highly obscured AGN (known as Compton thick (CT)) are lost in optical surveys and, to a lesser extent, in X-ray surveys as the radiation emitted at these frequencies is absorbed. These AGN could be detected in mid-infrared wavelengths, where obscuration effect are less important. However, their study in X-rays is fundamental to determine the obscuration level.

There are empirical relations in the literature that relate the mid-infrared and X-ray luminosity of AGN. The first objective of this work is to check whether these relations describe correctly the relation between luminosities for mid-infrared selected AGN samples (as the one used in this work) and to obtain our own relation otherwise. The second objective is to estimate a lower-limit for the obscuration for mid-infrared selected AGN not detected in deep X-ray exposures with the X-ray observatory XMM-Newton. The last objective is to estimate the necessary exposure times for the detection of this kind of objects with the X-ray observatories XMM-*Newton* and *Athena*.

To accomplish these scientific objectives we have selected a sample in the mid-infrared composed of 91 AGN: 68 detected in X-rays with XMM-*Newton*, 3 detected in X-rays but with low-quality X-ray spectra and 20 AGN with no X-ray detection. As it is a sample selected in the mid-infrared it is expected to include objects with obscuration levels all over the parameter space. These AGN (23) are our sample of CT candidates. The X-ray undetected AGN and those with low-quality X-ray spectra are expected to be highly obscured or CT. For the undetected AGN we have upper-limit estimated for their X-ray fluxes. For those AGN with low-quality X-ray spectra, we have the observed luminosity (not corrected by obscuration). These measurements will be used to put constrains on

the level of obscuration for these sources.

First, we obtained the intrinsic X-ray luminosity (corrected by obscuration) of the CT candidates. To do that we check if the empirical relations of the literature between X-rays and mid-infrared luminosities are valid for mid-infrared selected samples. As previous relations in the literature overestimate the X-ray luminosity of our sources we obtained our own empirical relation using the X-ray detected AGN in our sample. We obtained the intrinsic X-ray luminosity for the CT candidates assuming they follow the same relation as the X-ray detected AGN. Then the lower-limit of the obscuration of the AGN was estimated. We modelled their X-ray emission with a torus model and we used the intrinsic X-ray luminosity derived for every object from their mid-infrared luminosity. We ran simulations increasing the obscuration until the upper-limit flux or the observed luminosity was reached. Once we know the obscuration we estimated the exposure time needed to detect them with the X-ray observatories XMM-*Newton* and *Athena*. To do so we run new simulations with the same model imposing a signal-to-noise ratio threshold equal to 5 to accept the detection.

In this work we have found that: a) mid-infrared selected AGN are intrinsically weak in X-rays in comparison with X-ray selected AGN, consequently traditional empirical relations overestimate their intrinsic X-ray luminosity; b) the absorption of the CT candidates is high or even extreme is most objects; c) it is not possible to detect most obscured AGN with the actual generation of X-ray observatories in a reasonable exposure time; d) *Athena* will be able to detect such highly obscured AGN population routinely with the extragalactic surveys planned for the mission.

Key words: active galactic nuclei, column density, X-ray obscuration, XMM-*Newton*, *Athena*, detection

Contents

1. Introduction

1.1 Motivation

One of the great challenges for astronomy in the 21st century is to understand the formation and evolution of galaxies. This has been recognised by the strategic plan for astronomy of the European Union for the next 20 years, "A Science Vision for European Astronomy", where the formation and evolution of galaxies is one of the four fundamental questions of extragalactic astronomy. Also in the scientific objectives of the European Space Agency (ESA) "Cosmic Vision 2015-2025", supermassive black hole (SMBH) are identified as “the driving engines of the birth and evolution of galaxies [...] observations of these growing supermassive black holes along cosmic history will give unprecedented information on the growth of large-scale structures in the Universe and on the formation of galaxies”.

Nowadays there are clear evidences that most galaxies (probably all of them) have a SMBH in their centres 1, 2. If the SMBH is actively accreting material from the host galaxy is called an Active Galactic Nucleus (AGN). AGN have a hot accretion disk ($T \approx 10^6 - 10^7$ K) that emits large quantities of mainly ultraviolet and optical radiation as a consequence of the heating by the friction of the accreted material. Other structures reprocess this radiation, producing X-ray (corona) and infrared (torus) radiation.

The corona is a gas of hot electrons ($E = 10$ keV $- 1$ MeV) placed around the SMBH and the innermost part of the accretion disk. The photons from the disk may interact with the electrons of the corona and get promoted to higher energies through Inverse Compton scattering. The resultant X-ray radiation from the corona follows a power law, $f_\nu \propto \nu^{-\alpha}$, where f_ν the emitted flux at frequency ν and α the power law index. The other structure, the so-called torus, is a dust and gas toroidal structure around the nuclear region of the AGN (SMBH, accretion disk and corona). Photons from the disk and the corona are absorbed in the torus and re-emitted as infrared radiation. The whole picture of the AGN and these two structures can be seen in Figure 1.

One of the most surprising discoveries of the last 20 years was the finding of relations between the properties of SMBH and their host galaxies [3, 4, 5]. The strongest one is the parallel evolution in cosmic time between the star formation rate of the galaxies and the SMBH accretion rate [6], as can be seen in Figure 2. It

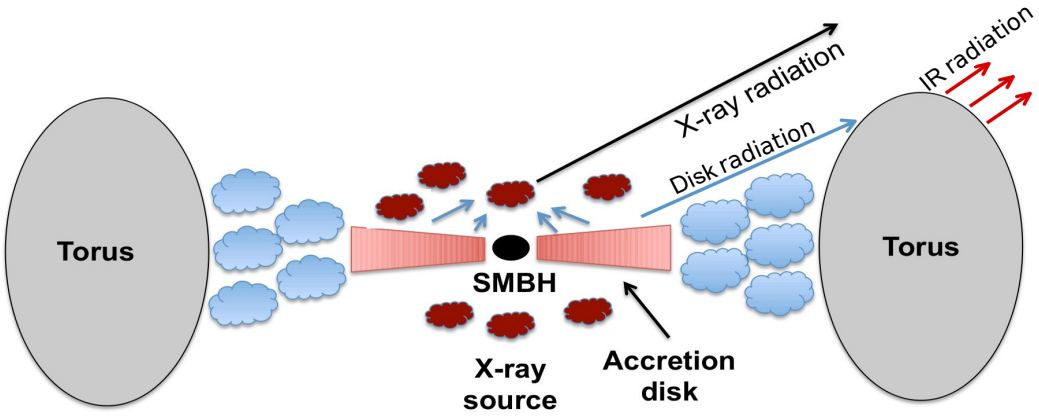

Figure 1: Scheme of the structure of an AGN. The black sphere is the SMBH. Next to it the accretion disk is depicted with red cones. The red clouds around are the corona and the grey ovals the torus. Blue clouds are the inner regions of the torus. The radiation from the accretion disk is re-emitted both by the corona as X-ray radiation and by the torus as infrared radiation. Adapted from Claudio Ricci personal web page: `http://www.isdc.unige.ch/~ricci/Website/Active_Galactic_Nuclei.html`.

is an unexpected result as galaxies have sizes of the order of kiloparsecs while SMBH is contained in a region of the size of the Solar System. These relations are suggesting that somehow SMBH and galaxy evolution goes hand in hand, either because of the influence of the SMBH over the galaxy, due to the influence of the galaxy on the SMBH or maybe because a third process is regulating both. So to fully understand galaxy formation and evolution we need to study the SMBH in their centres when they are in an active phase as AGN.

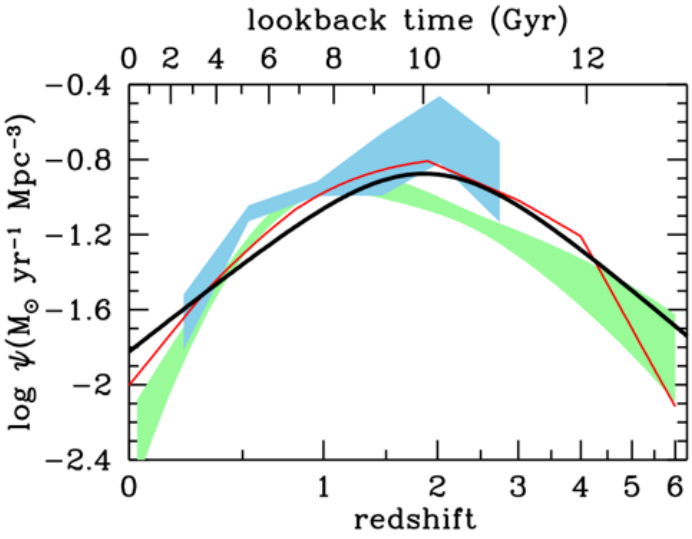

Figure 2: The history of star formation rate in galaxies versus redshift is represented as a black line. It is also represented the growth history of SMBH revealed by X-ray as both a red curve and a light green shading and by infrared surveys as a blue light shading. Obtained from Madau & Dickinson (2014) [6].

To explain the shape of the integrated emission of all AGN in the X-ray band (known as the cosmic X-ray background) most AGN have to be highly obscured [7], hindering their detection in the spectral range between the optical and the X-ray with energies $\lesssim 10$ keV. The traditional classification of AGN is based on whether the objects are absorbed or not by the torus. If our line of sight is blocked by the torus we will see an absorbed AGN or type 2. While if the line of sight is not blocked we will see an unobscured AGN or type 1.

The absorption suffered by an AGN is quantified using the column density, $N_{\rm H}$, which is a measure of the amount of matter between the observer and the radiation source, given as hydrogen-equivalent surface density of the dust and gas that absorb the radiation. $N_{\rm H}$ is usually given as hydrogen atoms per square centimetre [10]. An AGN is normally considered to be absorbed if it has $N_{\rm H} > 10^{22}$ cm^{-2} [11].

An AGN is defined as Compton-thick (CT) when its column density is higher than the inverse Thompson cross-section, $N_{\rm H} \geq \sigma_T^{-1} \approx 1.5 \times 10^{24}$ cm^{-2} [12]. At this point the Compton scattering and the photoelectric absorption are equally probable and the torus becomes optically thick for X-ray radiation below 10 keV. For extreme values of the column density ($N_{\rm H} \geq 10^{25}$ cm^{-2}, heavily Compton thick AGN) high energy X-ray emission is also absorbed. If $N_{\rm H} < 1.5 \times 10^{24}$ but is still larger than $N_{\rm H} > 10^{22}$ cm^{-2} then the AGN is known as Compton-thin AGN (Ct AGN) [12].

These strong absorptions make CT AGN difficult to detect and study since they are extremely faint not just in X-rays but at many wavelengths. Currently, it is not known how many CT AGN have escaped detection and their properties are largely unknown [13]. So, the study of the most obscured AGN, and particularly CT AGN, is a vital part to fully understand not only the history of the Universe and but also galaxy formation and evolution.

1.2 Detection of highly obscured AGN

AGN radiate at all wavelengths: from radio to X-ray [14]. As previously introduced, the accretion disk is the origin of most of the energy emitted by the AGN [15] and its re-emitted in the corona as X-ray radiation. Both, radiation from disk and corona, are also absorbed and re-emitted at infrared wavelengths by the torus. Radio emission comes from a jet of energetic particles (electrons and protons) with speed near to the speed of light which is present in a fraction of the sources

[14]. To search for obscured AGN we can use different techniques at different frequencies [13].

Optical and ultraviolet radiation is absorbed by the torus, thus searching for AGN at these wavelengths will miss the most highly obscured objects [14]. Radio emission is not absorbed and does not have contamination from host galaxy but only 15-20% of the AGN are bright enough at radio frequencies to be detected with current instrumentation [16]. Instead, mid-infrared and X-ray are promising avenues.

The mid-infrared[1] waveband provides efficient selection techniques of highly obscured AGN as infrared radiation suffers from much less absorption than other wavelengths [13]. Furthermore, even the most obscured AGN should be bright at mid-infrared wavelengths. Some of the techniques to select obscured AGNs at these wavelengths are:

- Identification of a significant emission from the AGN. It can be achieved from the detection of AGN features in the mid-infrared spectra (e.g. strong absorption caused by Si-based dust grains) or the fitting of the mid-infrared spectral energy distribution with AGN and host galaxy models. [13]
- Detection of high excitation lines, which cannot be explained by star formation processes, like [NeVI] at rest-frame 7.6 μm or [NeV] at rest-frame 14.3 μm. [17]
- In nearby galaxies the identification of a bright mid-infrared point source using high spatial resolution observations. [18]

The most common approach to identify AGN when only photometric observations are available is colour-colour diagrams [19, 20, 21, 22]. Mid-infrared colours are defined as the ratio between monochromatic fluxes[2] at different wavelengths, or as the difference between magnitudes[3]. Colour-colour diagrams take advantage of the different shape of the mid-infrared spectra for different objects. Figure 3 shows the distribution of colours for the most important classes of objects detected in mid-infrared. The colours are based on the three shortest wavelength filters

[1] In this work mid-infrared means wavelengths in the range $3 - 30$ μm.

[2] In astronomy the flux is defined as the incident energy per unit of area and time

[3] Magnitudes are defined as $m = -2.5 \times \log_{10}(\frac{f_{obj}}{f_*})$ with f_{obj} the flux of the object and f_* a reference flux

(W_1,W_2,W_3) from the Wide-Field Infrared Survey Explorer (WISE [23]).

Nonetheless, contamination from the host galaxy may hinder AGN identification. Because of this mid-infrared selection is only reliable for luminous AGN where AGN emission dominates over its host galaxy [13].

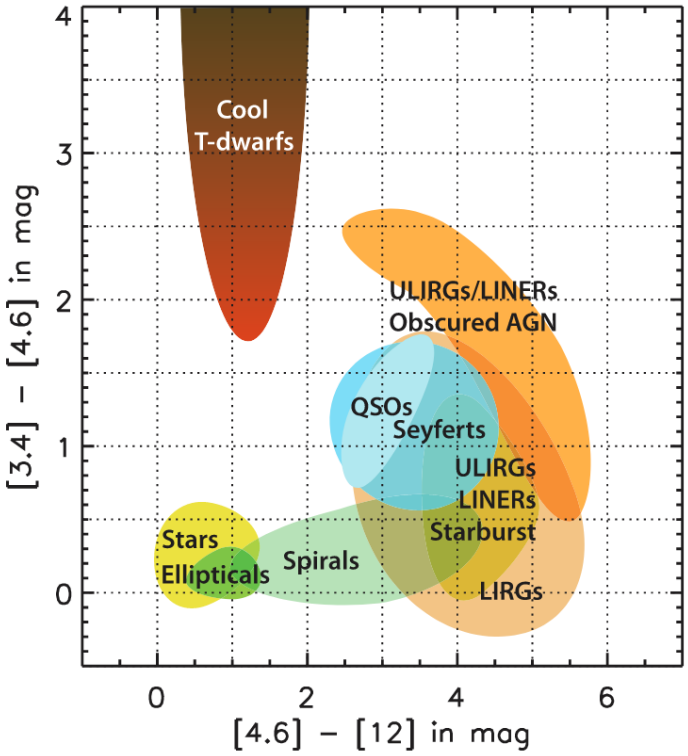

Figure 3: Mid-infrared colour-colour diagram for different population of objects based on W_1, W_2 and W_3. Right and up means redder colours. Stars are represented as yellow and brown areas, the horizontal branch of normal galaxies is represented in different shades of orange and green and AGN are represented as a blue area (QSOs and Seyferts). Taken from Wright et al (2012) [23].

X-ray selection of AGN is the most complete and reliable way to select AGN. Most sources detected at X-ray energies above 2 keV and outside the Galactic plane (Galactic latitudes higher than $|20^\circ|$) are AGN [24].

The most sensitive X-ray detectors currently in space work at energies below 10 keV but highly obscured AGN emission is largely absorbed at these energies. Furthermore, as introduced in Section 1, the direct X-ray emission from CT AGN is completely absorbed below 10 keV. In these cases, only the X-ray emission scattered by the torus is observed, which is $< 5\%$ of the direct emission [25]. This effect can be seen in Figure 4. So any X-ray selected AGN sample would be biased against the most highly absorbed AGN.

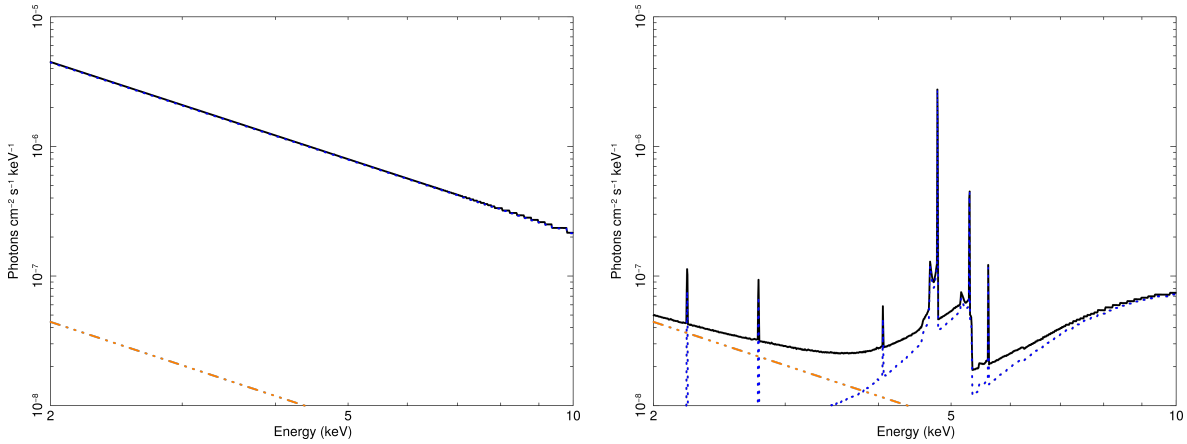

Figure 4: Simulated 2-10 keV emission of an AGN modeled with the BNTorus model – see Section 3.2 for details – and the scattering component. We use a redshift of $z = 0.334$ and $N_{\rm H} = 10^{20}$ cm^{-2} (left) and $N_{\rm H} = 1.5 \times 10^{24}$ cm^{-2} (right). The blue dotted represent the direct component, the orange dashed-dotted lines the scattering component and the solid black line the total emission.

1.3 Objectives of the work

We have a mid-infrared selected sample of 68 AGN with X-ray detection and 23 AGN without detection or low-quality X-ray spectra. We have: a) for the undetected at X-rays AGN the upper-limit of the X-ray flux at the 2-12 keV band; b) for the AGN with low quality X-ray spectra the observed X-ray luminosity[4], not corrected by absorption; c) the instrinsic luminosity (corrected by absorption) and the obscuration for detected AGN with high quality spectra. Undetected and low quality spectra AGN are expected to be heavily obscured. The main objectives of this work are:

- Verify whether the previously reported relations between X-ray intrinsic luminosity and mid-infrared luminosity describe properly mid-infrared selected samples of AGN.

- Obtain a relation between the mid-infrared and X-ray luminosities for mid-infrared selected AGN samples to estimate their intrinsic X-ray luminosity.

- Obtain a lower-limit or and estimation to the obscuration and the number of CT candidates for not X-ray detected and low-quality X-ray spectra AGN respectively.

[4]In astronomy, the luminosity of an object is the amount of energy radiated per unit of time

- Determine whether these objects could be detected using the X-ray observatory XMM-*Newton* (increasing the exposure times) and how much time they will take to be detected with *Athena*.

Through this work, we use the cosmological parameters $H_0 = 70\,\mathrm{km\ s^{-1}\ Mpc^{-1}}$, $\Omega_\mathrm{M} = 0.3$ and $\Omega_\Lambda = 0.7$ to allow a direct comparison with other works in the literature.

2. Instrumentation and sample description

In this section, we introduce all the information that makes up the starting point of the work. First, we describe the space observatories used: The Wide-field Infrared Survey Explorer, X-ray Multi-mirror Mission - *Newton* and *Athena*. We also introduce the properties of the surveys carried out with them. Then we define the AGN sample used in this work, its properties and the process used to remove host galaxy contamination at mid-infrared wavelengths to derive the mid-infrared AGN luminosities of our sources.

2.1 Infrared instrumentation

In this work we have used observations from the Wide-field Infrared Survey Explorer (WISE). WISE is a NASA mission launched in January 2010 to survey the sky in the mid-infrared band. WISE has four filters centred at 3.4 μm (W_1), 4.6 μm (W_2), 12 μm (W_3) and 22 μm (W_4) [23].

The two filters working at the longest wavelengths need low temperatures to work and because of the exhaustion of the cryogenic material, since August 2010 WISE works only with the two shortest wavelength filters. But before that date WISE was able to map all the sky, leading to the publication of the *All Sky Data Release Source Catalogue* in 2012 [26]. This catalogue was used in this work and is available at `http://wise2.ipac.caltech.edu/docs/release/allsky/`.

All detections in the *All Sky Data Release* have at least a signal to noise ratio (SNR, see Section 3.3 for details) of 5 in at least one of the filters. WISE has achieved good point source sensitivities (5σ sensitivities better than 0.08, 0.11, 1 and 6 mJy[5] in W_1, W_2, W_3 and W_4, respectively) and angular resolution (FWHMs of 6.1", 6.4", 6.5", and 12.0" in W_1, W_2, W_3 and W_4, respectively) and positional accuracies below 0.15 arcsec for high SNR sources (SNR>20) [23, 26].

2.2 X-ray instrumentation

2.2.1 X-ray Multi-mirror Mission - Newton

X-ray Multi-mirror Mission - Newton (XMM-*Newton*) is an observatory of the European Space Agency (ESA) launched on the 10 December 1999 to study the

[5]The Jansky (Jy) is a unit of flux defined as 1 Jy $= 10^{-23}$ erg s^{-1} cm^{-2} Hz

X-ray sky. Nowadays, 20 years after its launch, XMM-*Newton* is still operational. XMM-Newton is composed of three telescopes, each one with a camera that together compose the European Photon Imaging Camera (EPIC). Two cameras were developed using Metal Oxide Semi-conductor (MOS) CCD technology and one was developed with pn CCD technology. Each MOS camera shares the incident light with a reflection grating spectrometer (RGS). Consequently, for the same exposure time, the EPIC-pn camera provides the deepest observations [27].

Everytime XMM-*Newton* makes an observation, inside the EPIC camera field-of-view (approximately 30x30 arcminutes [28]) around 30-100 objects are detected, most of them being AGNs. This can be seen in Figure 5. To manage this amount of information and to provide X-ray source catalogues for the astronomical community the Survey Science Centre (SSC) was set up by ESA [29].

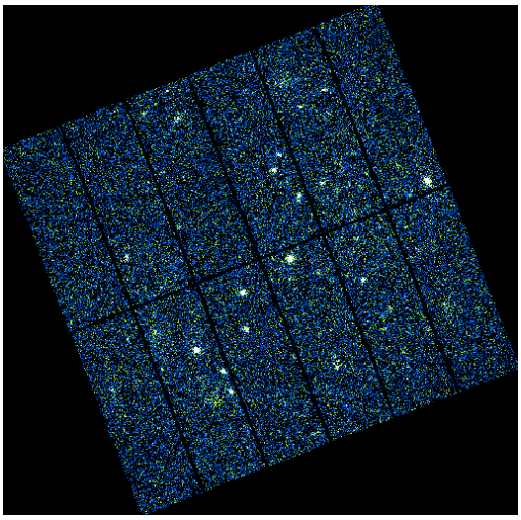

Figure 5: Example of an observation with the EPIC-pn camera. The bright blobs are AGN detected at the same time as the target object (located at the center of the field-of-view). Adapted from the XMM-*Newton* Science Archive: `https://nxsa.esac.esa.int/nxsa-web`.

SSC publishes periodically serendipitous source catalogues for the EPIC camera. The SSC uses only observations of a quality suitable for the detection of those sources. These catalogues are known as the XMM-*Newton* Serendipitous Source Catalogues. In this work we have used the eigth revision of the third XMM-*Newton* Serendipitous Source Catalogue (3XMM-DR8) released in 2017 [30]. The catalogue can be found at `http://xmmssc.irap.omp.eu/Catalogue/3XMM-DR8/3XMM_DR8.html`

XMM-*Newton* observes the sky in the energy range $0.5 - 12$ keV but this range is actually splitted in five energy bands for source detection: $0.2 - 0.5$ keV, $0.5 - 1.0$

keV, $1.0 - 2.0$ keV, $2.0 - 4.5$ keV and $4.5 - 12.0$ keV. 3XMM-DR8 identifies a detection when the likelihood total-band of of a detection is, $L' = \sum_{i=1}^{N} L_i$, is above 5 [30, 31]. In the previous equation L' is the total-band likelihood and L_i the likelihood for every of the five bands.

If a detected object is off-axis – i.e. outside the pointing position of the telescope – we will have worse quality measurements. This is due to the mirror *vignetting*: with an increasing off-axis angle fewer photons reach the focal plane [32]. The fraction of lost photons (that is also a function of the energy of the incoming photons) is quantified as an effective exposure time that decreases at larger off-axis angles. This is represented in the so-called exposure maps, such as the one shown in Figure 6. If the object is highly off-axis the properties measured (coordinates, fluxes...) will typically have larger uncertainties.

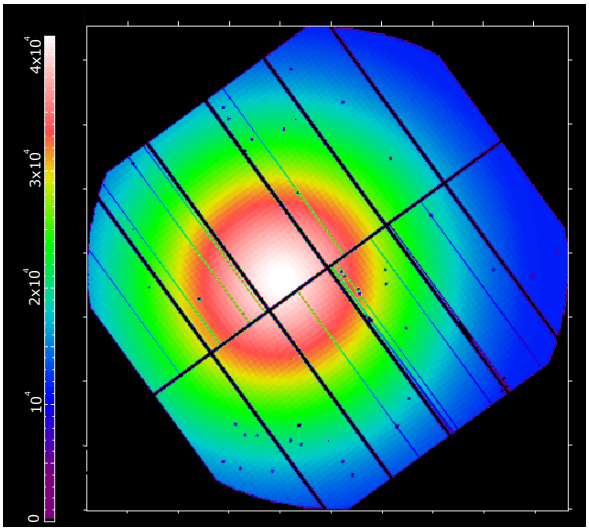

Figure 6: Example of an exposure map from the EPIC-pn camera illustrating the spatial efficiency of the instrument. The brighter the colour is, the more net exposure time for the EPIC-pn camera in seconds (see the scale on the left of the figure). The maximum effective time will be achieved at the pointing position of the telescope. Obtained from: `https://nxsa.esac.esa.int/nxsa-web/`

As indicated before, for our X-ray undetected AGN we have upper-limits for the X-ray fluxes. To compute them we have used the task *eregionanalyse*[6] task. It uses the background level and the exposure at the position of the sources (the mid-infrared coordinates) to obtain the 1σ upper-limit of the number of counts per unit of time that arrive at the detector from the source, the so-called count rate.

[6] A detailed description of the task can be found in `https://heasarc.gsfc.nasa.gov/docs/xmm/sas/help/eregionanalyse/index.html`

2.2.2 Athena

Athena is an L-class mission of ESA to study the hot and energetic universe [33] via X-ray observations. The main scientific goals are [34]:

- Determine how large-scale hot gas structures formed in the Universe and track their evolution from the formation epoch to the present day.
- Perform a complete census of black hole growth in the Universe, determine the physical processes responsible for that growth and its influence on larger scales, and trace these and other energetic and transient phenomena to the earlier cosmic epochs.
- Provide a unique contribution to astrophysics in the 2030s by exploring high energy phenomena in all astrophysical contexts, including those yet to be discovered.

Athena was selected as an ESA mission on June 2014 and it is expected to be launched in 2031. The mirror of Athena have a Half Energy Width (HEW) of 2.5″. To accomplish its objectives *Athena* will be equipped with two instruments: the X-ray Integral Field Unit (X-IFU) and the Wide Field Imager (WFI).

The X-IFU will be an advanced X-ray cryogenic calorimeter spectrograph for high resolution observations based on a large array of Transition Edge Sensors (TES). The X-IFU will have an spectral resolution of 2.5 eV in the range $0.2 - 12$ keV. In comparison, the EPIC-pn camera of XMM-*Newton* has a spectral resolution of 80 eV, 32 times worse [35, 36]. X-IFU will focus in obtaining high-quality spectra of bright targets.

The WFI will be a very powerful instrument to carry out surveys with different depth and area. It will work in the range $0.2 - 15$ keV providing imaging simultaneously with spectrally and time-resolved photon counting. WFI has a 40'x40' field-of-view. WFI relies on the DEPFET technology of active pixels allowing to reach the noise limit due to the fluctuation of electric charge [34, 37]. As every pixel is read individually, the WFI will reach a temporal resolution of 10 μs, while the XMM-*Newton* EPIC-pn camera reaches a temporal resolution of 30μs.

The WFI will surpass all modern CCD-based X-ray instruments. In Figure 7 we can see a comparison between the effective area for the *Athena* WFI and two of the most used instruments of the current generation, XMM-*Newton* EPIC-pn and

Chandra ACIS-I [38]. *Athena* clearly will surpass them, obtaining a factor x10 in the effective area in comparison with the EPIC-pn camera.

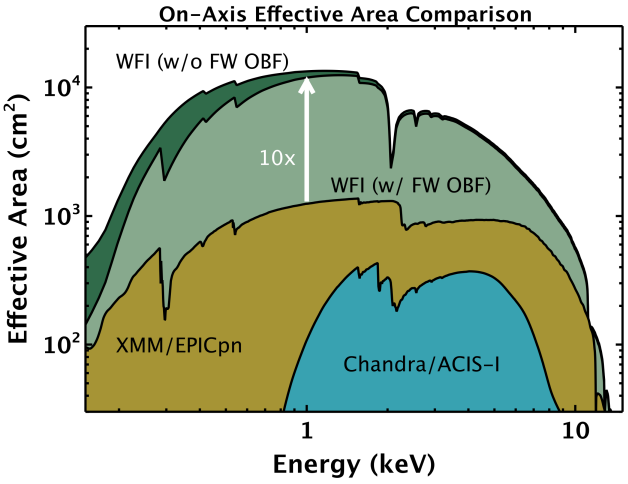

Figure 7: Comparison between the effective areas of the *Athena* WFI camera (with and without Filter Wheel Optical Blocking Filter), XMM-*Newton* EPIC-pn camera and Chandra ACIS-I camera. *Athena* has by far the greatest area. Obtained from `https://www.the-athena-x-ray-observatory.eu/resources/gallery/wfi.html`.

2.3 WISE Sample

To select our AGN sample we have relied on the *All Sky Data Release* catalogue from WISE. Our AGN selection technique is the colour-colour diagram from Mateos et al. (2012) [21]. To build the AGN sample used in this work a 12 μm flux limit of $f_{12\ \mu m} > 1$mJy was imposed to select sources sufficiently bright to make sure we are selecting AGN using the colour-colour technique. These AGN were selected in the sky areas with deep observations with XMM-*Newton* ($t_{obs} > 45$ ks).

The colour selection from Mateos et al. (2012) is based on the three shortest wavelengths WISE filters and defines the selection as a 2D region: all objects inside the "AGN-wedge" are candidates to be AGN. The selection region and the position in the diagram of our AGNs candidates are represented in Figure 8. Using this colour-colour diagram we obtain 96 AGN candidates. We have 91 candidates with optical spectra from which we have obtained the redshift. This is the sample of objects we have used in this work. For 81 of those we were able to check that they are AGN using optical spectroscopy (detection of broad emission lines or high ionization emission lines), detection in X-rays or SED analysis (modelling emission with AGN and host galaxy components). The rest (10 objects) are highly probable to be AGN: the colour selection has low contamination and the SED of the ten objects can not be explained with only a galaxy model, see Section 2.4 for details. Nevertheless, we would need more observations to obtain a direct

confirmation of their AGN nature (like near-infrared spectra).

We used XMM-*Newton* observations to constrain the X-ray properties of our sources. This is a distinctive feature of our sample as no other mid-infrared selected sample at similar fluxes has so deep observations in X-rays.

- 68 AGN have X-ray detection and good enough quality spectra to constrain their obscuration.
- 3 AGN X-ray have detection and low-quality spectroscopy that does not allow to recover their obscuration.
- 20 AGN have no X-ray detection.

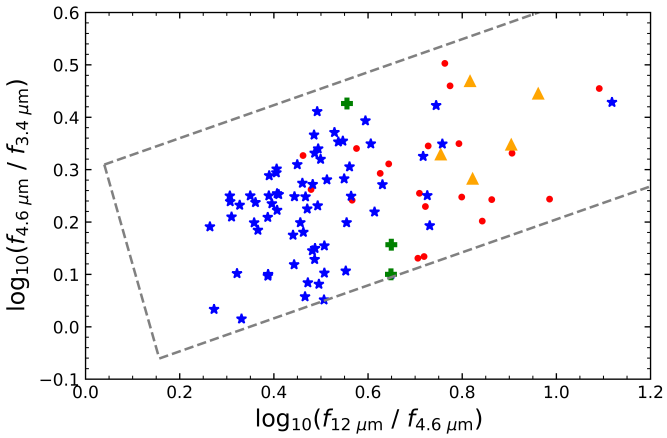

Figure 8: Colour-colour diagram the 96 mid-infrared selected AGN. We represent with blue stars the AGN with X-ray detection, with red dots the AGN without X-ray detection, with green crosses the AGN with low-quality spectra (together they constitute the sample used in this work) and with orange triangles the objects without optical spectra. The AGN selection wedge from Mateos et al (2012) [21] is represented with grey dashed lines.

No CT AGN have been found among the X-ray detected AGN so we look for CT candidates in the 23 AGN without detection and the 3 AGN with low-quality X-ray spectroscopic data as we are expecting them to be highly obscured AGN. Hereafter this subsample of 23 AGN will be referenced as simply CT candidates while the 91 AGN with optical spectra will be referenced as the *WISE full sample*.

The optical classification of our CT candidates is as follows: 18 objects are classified as type 2 AGN (78% of the sample) while 5 of them are type 1 AGN (22% of the sample). That most of the sample are type 2 AGN (optically obscured AGN) is suggesting us that we are most likely selecting highly obscured objects [39]. Generally, type 1 AGN have low absorption but maybe our selection is identifying highly obscured type 1 AGN as well.

Every X-ray observation of AGN without spectra has a 1σ upper-limit of the count rate in the $2-12$ keV energy band associated with it, among other parameters. For them we will use the 1σ upper-limit count-rate to estimate the minimum absorption the AGN may have. For the 3 AGN with low-quality spectra we instead have their observed (not corrected by torus absorption) X-ray luminosity in the $2-10$ keV energy range, obtained from a basic analysis of their spectra. Finally for detected AGN with good quality spectra we have estimates of their intrinsic (absorption corrected) luminosity and column density.

2.4 Mid-infrared luminosity estimates

The estimation of the mid-infrared luminosity and the subtraction of host galaxy contamination is a key step on the preparation of the sample, and very important to have quality results. Because of that, although this work have been done by partners of the group, it is explained in detail in this section.

We obtain the monochromatic luminosity at rest-frame 6 μm, $L_{6\ \mu\mathrm{m}}$[7], using the photometric data from WISE. First, the flux at 6 μm was computed using a linear interpolation in log-log space. This is possible because at these wavelengths the emission can be approximated as a power law [40]. Then it is trivial to obtain the luminosity at 6 μm using the redshift and the cosmology parameters introduced in Section 1.3.

Dust from stellar formation regions (heated by UV radiation of young stars) emits infrared radiation and it could be a serious contaminant of our $L_{6\ \mu\mathrm{m}}$ estimates. In this work it is expected not to be the case: when the contamination from host galaxy emission is large the objects should have mid-infrared colours outside the AGN wedge. Nonetheless, we have estimated the maximum possible contribution of our AGN hosts to $L_{6\ \mu\mathrm{m}}$. This way we are following a conservative approach assuming the worst case scenario.

We compare the photometric SEDs of our sources (from optical and infrared wavelengths) with the host galaxy models from Kirkpatrick et al. (2012) [41]. These models are composite spectral energy distributions derived from a sample of 95 star-forming galaxies with complete coverage at infrared wavelengths. Our photometric data are the same as in [39]. We increase the galaxy contribution until

[7]The monochromatic luminosity is defined as λL_λ in erg s^{-1}, using here $\lambda = 6\mu m$. Nonetheless we will refer it as $L_{6\ \mu\mathrm{m}}$

one of the infrared fluxes derived from the galaxy template equals the observed flux for our sources. Once reached this situation we interpolated the λf_λ at $\lambda = 6$ μm in log-log space using the galaxy templates. Is then trivial to obtain the monochromatic luminosity of the galaxy at $\lambda = 6$ μm. We use these values as conservative estimates for the contribution from the hosts for each AGN. An example of this procedure is presented in Figure 9.

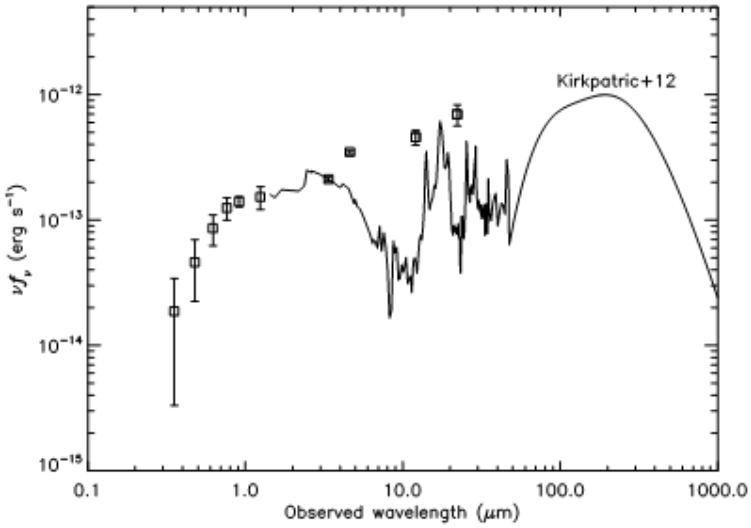

Figure 9: *Example of the SED of one of our objects (open squares) with the galaxy template from Kirkpatric et al. (2012) [41] (solid line). In this case, the limit in host galaxy emission is imposed by the WISE flux at 3.4*μ*m.*

In all cases, the corrections by the host galaxy are small. This is expected as the AGN wedge selects preferably luminous AGN. On average, the AGN contribution at rest-frame 6μm is 60% (individual values of observed and AGN mid-infrared luminosities are in Appendix A) which is in agreement with the results from Brown et al (2019) [42]. From this point on $L_{6\ \mu m}$ will refer to the AGN luminosity, i.e., corrected for the host galaxy contribution.

The distribution of $L_{6\ \mu m}$ versus redshift can be seen in Figure 10. The infrared luminosity of our sample covers 3 orders of magnitude. Most of the CT candidates have high infrared luminosity. For 22 AGN (96% of the sample) its $L_{6\ \mu m}$ is higher than 10^{43} erg s^{-1} and for 13 AGN (57% of the sample) its $L_{6\ \mu m}$ is higher than 10^{44} erg s^{-1}. So our 23 AGN are not only highly obscured but they are also very luminous.

In Appendix A a table with all the relevant data – sample ID, source number, redshift, classification, AGN infrared luminosity and intrinsic X-ray luminosity derived from the spectrum – for the WISE full sample can be found.

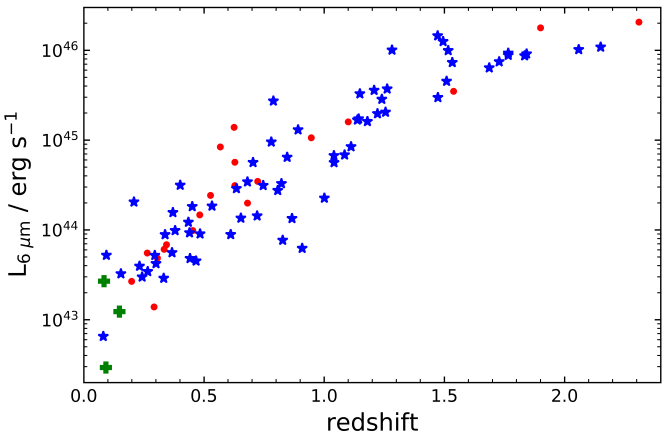

Figure 10: Infrared luminosity versus redshift. AGN without X-ray detection are represented as red dots, AGN with low-quality spectra are represented as green crosses and X-ray detected AGN are represented as blue stars.

3. Methodology

In this section, several concepts and tools commonly used in X-ray astronomy are introduced to allow a better understanding of the analysis carried out. XSPEC, SNR and the torus model among others will be introduced and explained.

3.1 XSPEC, RMF y ARF

Current X-ray spectra have a quality limited by technology. To be able to do a spectral analysis we need a flexible tool able to work with these limitations performing fits, simulating... In response to that need, XSPEC was developed by Keith Arnaud, Ben Dorman and Craig Gordon, members of the HEASARC Software Development of NASA [43]. XSPEC is nowadays the most used software to analyse X-ray data, model them and simulate new data from models.

XSPEC is a reliable software that allows a flexible approach to model the emission of a certain object using a simple coding language. XSPEC has a large library of models: power-laws, photoelectric absorption... All of them can be consulted at `https://heasarc.gsfc.nasa.gov/xanadu/xspec/manual/Models.html`. XSPEC can also import models from external files. Furthermore, XSPEC allows to sum and multiply different models, allowing to describe complex emission as the combination of several simpler absorption and/or emission processes. Once the observed data is properly modelled, XSPEC allows recovering fluxes, luminosities and count rates (in different ranges) as well as line of sight X-ray absorption, among other quantities.

To model the emission of an object detected by an telescope XSPEC uses the redistribution matrix file (RMF) and the auxiliary response file (ARF). The RMF associates the instrumental channels with the energy of the incoming photons while the ARF describes the combined "effective area" of the telescope, filter of the observation and detector as a function of energy [44, 45].

Nonetheless, XSPEC scripting is not flexible. To overcome this problem we rely on PyXspec[8], a python implementation of XSPEC developed by Keith Arnaud and Craig Gordon. In this work, XSPEC has been used through PyXspec.

[8]Documentation of PyXspec can be found at `https://heasarc.nasa.gov/xanadu/xspec/python/html/index.html`

3.2 Torus model

To simulate the X-ray emission that best represents our CT candidates we need a model that takes into account the absoprtion, scattering and reflection of the direct emission from the corona (see Section 1) by the material of the torus. Several torus models have been developed in the last decade like those from Murphy & Yaqoob (2009) [46] or Baloković et al. (2018) [47].

In this work, we use the torus model from Brightman and Nandra (2011) [48], commonly known as BNTorus. This is a traditional choice used commonly in other works in the literature [49, 50, 51]. The BNTorus is a table model, i.e., the model has all the relevant properties of the emission calculated for certain values of the free parameters. For any intermediate value, it extrapolates between them. BNTorus has 6 free parameters:

- Column density of the torus, N_{H} (see Section 1 for details).
- Photon index of the X-ray power law, Γ. As introduced in Section 1, the X-ray direct emission from the corona follows an power law spectrum. It can be described using the photon index, Γ, as $\nu f_\nu \propto \nu^{-(\Gamma-1)}$. In our work we have used $\Gamma = 1.9$, the typical value found for AGN [52, 53, 54].
- Aperture angle of the torus, α, that describes the amount of sky obscured and is defined from the polar axis (see Figure 11). In our work we have used $\alpha = 40^{\mathrm{o}}$.
- Viewing angle, i, defined from to the polar axis (see Figure 11). In our work we have used $i = 80^{\mathrm{o}}$ to ensure that the line of sigth is blocked by the torus.
- Redshift of the AGN, z.
- Normalization of the emission, N, related to the intrinsic luminosity of the AGN. It corresponds with the monochromatic photon flux at 1 keV.

We also need to take into account the scattering component which is not included in the BNTorus. It is the X-ray radiation scattered by the material inside the torus to the line of sight direction. It follows an unabsorbed power law spectrum with the same photon index as the direct emission but it is less intense. Its mean value for absorbed AGN is 1% of the direct X-ray emission [55]. We model it with the same redshift and normalization equal to $0.01N$.

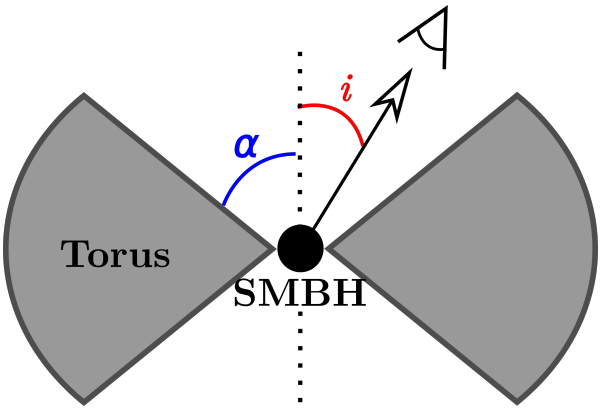

Figure 11: Representation of the aperture angle of the torus, α, and viewing angle, i, in the context of the BNTorus model. The vertical dotted line represents the polar axis.

3.3 Signal-to-noise ratio

The signal-to-noise ratio (SNR) is a traditional way to describe numerically the confidence of a certain detection. The SNR is defined as the ratio between the signal S and the noise R [56]:

$$\mathrm{SNR} = \frac{S}{R} \tag{1}$$

As we are counting incident photons we are working in a Poisson regime. But if we have enough photons (usually $n > 20$) we use a Gaussian approximation. In this work, we do all our computation assuming we are working in a Gaussian regime. Our signal, S, would be the difference between the total counts, T, and the background counts, B, $S = T - B$ and its noise $R^2 = \sigma_s^2 \approx \sigma_T^2 + \sigma_B^2$. The noise of photons arriving at random in this regime is:

$$\sigma_T = \sqrt{T} \rightarrow \sigma_T^2 = T \tag{2}$$

In the same way, the source and background noise are defined as $\sigma_S^2 = S$ and $\sigma_B^2 = B$. If we assume a source count rate m and a background count rate b we can obtain the SNR at a certain exposure time, t, as:

$$\mathrm{SNR} = \frac{S}{R} = \frac{T - B}{\sqrt{T + B}} = \frac{m \times t + b \times t - b \times t}{\sqrt{m \times t + b \times t + b \times t}} = \frac{m}{\sqrt{m + 2b}}\sqrt{t} \tag{3}$$

and the exposure time needed to obtain a certain SNR given m and b is:

$$t = \mathrm{SNR}^2 \, \frac{m + 2b}{m^2} \tag{4}$$

In this work we will use SNR = 5 as the threshold to accept the detection of an object, as in the WISE mission [26].

3.4 PSF, EEF and Backscale

The point spread function (PSF) describes the 2-dimensional distribution of light in a certain telescope focal plane for a point source [57]. The PSF depends on the off-axis angle and the photon energy [58]. The PSF of a perfect instrument is an Airy pattern which can be approximated as a 2D Gaussian function. For XMM-*Newton*, there were several 1D descriptions of the PSF (King profile 3-Gaussian, Parametrization...) until Read et al. (2011) obtained a 2D representation of the PSF across the full field-of-view using the stacking and centring of bright point sources [59].

Another way to quantify the angular resolution is the Half Energy Width (HEW). HEW is defined as the diameter within which half of the energy of a source is recovered. Assuming a radial symmetric PSF:

$$1/2 = \int_0^{HEW/2} \mathrm{PSF}(r)\mathrm{d}r \tag{5}$$

where $\mathrm{PSF}(r)$ is normalized to 1. Related with the PSF is the encircled energy fraction (EEF). The EEF is the fraction of the total integrated flux in the image of a source within a given radius R [57]. It is trivial to obtain the EEF for a certain energy as:

$$\mathrm{EEF}(r) = \int_0^{r} \mathrm{PSF}(r)dr \tag{6}$$

Every time we measure the count rate of a source we have to take into account the EEF. This way, if we have observed a count rate s from a source within a radius r the total count rate, s_0, is:

$$s = s_0 \times \mathrm{EEF(r)} \tag{7}$$

Another important effect to take into account during observation is the *backscale*. To determine the source parameters the area used to extract the total (source plus background) counts and to average the exposure time is defined as the one that maximizes the SNR. Instead, to accurately measure the background the bigger the area the better but always in an area near to the object, as the background varies across the field-of-view. Consequently, the background extraction area is different from the source extraction area. To correct it we add a scale factor. So if b is the count rate in the background area and b_0 is the estimated background count rate

in the source area:

$$b_0 = \frac{A_{src}}{A_{back}} \times b \tag{8}$$

being A_{back} and A_{src} the areas for the background and source, respectively.

4. Results

As explained in Section 1.3 the main goals of this work are: a) check whether previous relations between X-ray intrinsic and mid-infrared luminosities describe properly mid-infrared selected samples, b) obtain X-ray intrinsic luminosities for CT candidates, c) estimate a lower limit of their obscuration and determine the number of CT AGN, d) compute whether these objects could be detected with XMM-*Newton* using reasonable exposures and the exposure time needed to detect them with *Athena*. In this section, we explain in detail the analysis carried out to achieve the above mentioned goals and we present the main results of the study.

4.1 Obtaining L_X

To obtain the obscuration of our CT candidates we need first to constrain their intrinsic X-ray luminosity. To do so we use the well known tight correlation between mid-infrared and X-ray luminosities. There are several empirical relations in the literature for both bright-nearby AGN (Lultz et al. (2004) [60], Gandhi et al. (2009) [61], Asmus et al. (2015) [62], Mateos et al. (2015) [63]) and faint distant AGN (Stern (2015) [64], Chen et al. (2017) [65]).

The first step was to check whether the relation from Chen et al. (2017) describes well our sample, i.e., whether the relation is valid for mid-infrared selected AGN. We start our analysis using Chen relation because our objects are weak (low X-ray fluxes) and non-local. Furthermore, we want to be conservative: for $L_{6\mu m}$ we want the relation that returns the lowest L_X and consequently the lowest N_H.

To do so we used the AGN with high-quality X-ray spectra (68 AGN, see Section 2.3) since for these objects we have robust estimates for both mid-infrared and X-ray luminosities. As shown in Figure 12 our AGN are systematically below the relation. If we use the Stern (2015) relation instead of the Chen et al. (2017) relation the situation is the same. This is telling us that a mid-infrared selection identifies X-ray weak AGN in comparison with X-ray selected AGN, used to calibrate the empirical relations of Chen (2017) [65] and Stern (2015) [64].

Thus we decided to use our X-ray detected AGN as a calibration sample to derive an empirical relation for mid-infrared selected AGN. Using the method of least squares we obtain the best fit of the points to a lineal relation in log-log scale, obtaining $\log_{10}(L_X) = 0.854 \times \log_{10}(L_{6\mu m}) + 7.952$. Our relation is also shown in Figure 12.

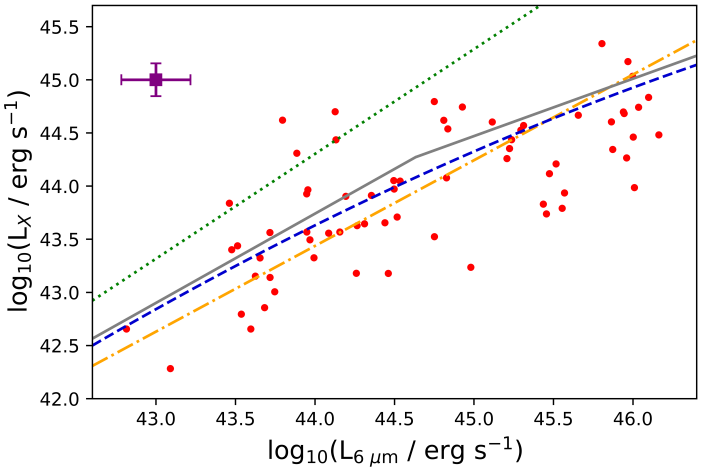

Figure 12: AGN infrared luminosity versus X-ray luminosity for the WISE-selected AGN with X-ray detection (red dots). We also show the empirical relations from Chen et al. (2017) [65] (grey solid line), Stern (2015) [64] (blue dashed line), Mateos et al. (2015) [63] (green dotted line) and our own relation (orange dashed-dotted line). The purple point at the top left of the figure shows the mean error for L_X and $L_{6\ \mu m}$.

We would have a mean overestimation for L_X of 37.30% if we use the Stern relation and the overestimation increases to 77.61% if we use the Chen et al. (2017) relation. This is showing the importance of checking the reliability of the above mentioned empirical relations for AGN samples covering different ranges of the parameter space (e.g., X-ray fluxes from Chen et al. (2017) [65]) and built from selections carried out at different wavelengths (e.g., mid-infrared vs. X-rays). If these issues are not taken into account this could lead to overestimations of both X-ray luminosity and line-of-sight absorption, resulting in the wrong identification of Compton-Thin AGN as Compton-Thick AGN. More on this topic can be found in Section 5

Using our empirical relation we obtain the intrinsic X-ray luminosity for the CT candidates assuming they follow the same behaviour as the rest of the sample. Figure 13 shows the intrinsic X-ray luminosity vs. redshift for our CT candidates. It shows that the sample covers a wide range in X-ray luminosity, about three orders of magnitude ($10^{42} - 2 \times 10^{45}$ erg s^{-1}), with just 4 AGN with X-ray luminosity below 10^{43} erg s^{-1}.

In table 1 the numerical values of the intrinsic X-ray luminosity for CT candidates are presented.

4.2 Column density determination

The process followed for the estimation of the column density for the Compton-thick AGN candidates is explained in this section. If the AGN have no spectra we

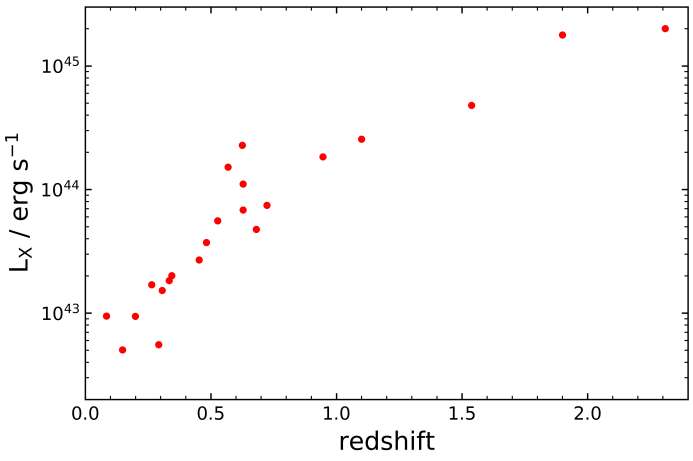

Figure 13: *Intrinsic X-ray luminosity estimated for the non-detected and low-quality X-ray spectra AGN against redshift.*

obtained a lower-limit for the obscuration. If we were able to obtain a low-quality spectrum we followed a different approach to estimate the obscuration. The two are explained in different sections to facilitate the reading.

4.2.1 AGN without X-ray spectra

To determine the column density for our AGN without spectra we rely on the estimation of the intrinsic X-ray luminosity and our 2-12 keV count rate upper limits. To model the X-ray emission we use the BNTorus torus model from Section 3.2 to be able to directly compare our results from others in the literature. As we are assuming a certain model our results will be model dependent.

First, the normalization has to be determined. We set the normalization so that intrinsic X-ray luminosity obtained from the model (i.e., $N_{\mathrm{H}} = 0$) is the one obtained from the corresponding infrared luminosity.

As we saw in Figure 4, an increase of the column density leads to a progressive decrease of the observed flux and count rate and a significant change of the shape of the spectra. An unobscured AGN shows just a broad-band power-law continuum but, when the column density is high enough the direct emission of the AGN decreases and the scattering component becomes much more important and several emission lines associated with Fe, Ni, Cr, Ca, Si and Ne become visible, being the most intense the Fe Kα at rest-frame 6.4 keV. To estimate N_{H} we simply increase its value until the count rate predicted by the model is equal or less than the count rate upper limits. As the count rate is an upper limit, the column density obtained is a lower limit.

AGN ID	**z**	**Class**	$\log_{10}$($\mathbf{L_X}$ / **erg s**$^{-1}$)	$N_{\rm H}$ / **cm**$^{-2}$	$\mathbf{t_{obs}}$ / **ks**	$\mathbf{t_{XMM}}$ / **ks**	$\mathbf{t_{Athena}}$ / **ks**
3	1.100	1	44.41	23.90	24.1	194.3	9.3
7	1.900	1	45.25	24.65	19.8	246.4	7.1
34	0.334	2	43.26	23.60	20.3	711.2	9.2
56	0.482	2	43.57	23.90	16.2	2268.0	14.8
58	0.681	2	43.68	23.60	15.0	459.6	14.1
66	0.148	2	42.70	24.05	59.0	275.4	9.0
98	2.309	1	45.30	24.20	16.1	427.8	5.4
105	0.453	2	43.43	23.75	26.4	2144.3	15.1
112	0.723	2	43.87	20.00	9.2	18.5	0.2
113	0.292	2	42.75	23.45	18.9	904.36	22.2
117	0.628	2	43.83	23.60	12.0	937.0	7.8
121	0.306	2	43.18	22.70	11.2	93.6	1.8
131	0.625	2	44.36	24.05	23.9	490.1	4.0
133	0.344	2	43.30	22.70	4.3	132.3	1.7
135	0.264	1	43.23	24.05	31.6	1845.9	9.4
136	0.199	2	42.97	23.90	30.6	434.7	8.3
139	0.527	2	43.75	23.45	18.0	698.8	5.2
143	0.084	2	42.98	26.00	48.0	154.6	1.3
173	0.092	2	42.20	24.50	31.5	611.8	11.4
188	1.538	1	44.68	24.50	44.8	727.9	20.3
199	0.946	2	44.26	24.35	51.9	1092.4	18.2
200	0.568	2	44.18	23.90	34.8	184.7	4.3
240	0.628	2	44.04	24.05	30.1	2280.6	9.2

Table 1: Column 1: sample identifier of the AGN; column 2: redshift of the AGN; column 3: classification following the same notation as Table 5; column 4: intrinsic X-ray luminosity in logarithmic units obtained from our empirical relation; column 5: lower-limit of the column density in logarithmic units (see Section 4.2); column 6: effective exposure time of the XMM-*Newton* observations; column 7: lower-limit of the exposure time needed to detect the objects with XMM-*Newton* (see Section 4.3.1); column 8: lower-limit of the exposure time needed to detect the sources with *Athena*, (see Section 4.3.2).

Energetic enough X-rays ($E > 10$ keV) can cross the torus being unaffected by absorption. Consequently, redshift will play a big role. At higher redshift we observe higher rest-frame energies at the observed frame 2-10 keV. Then at higher redshift, we see radiation less affected by obscuration, as illustrated in Figure 14. The redshift of the model is the one obtained from optical spectra.

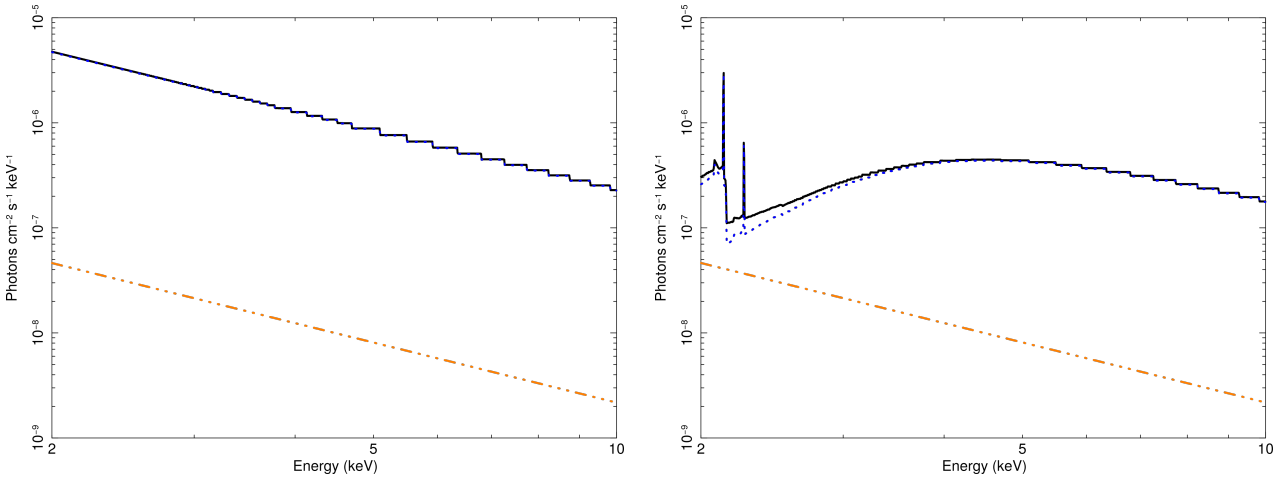

Figure 14: Simulation of the emission of an AGN in the 2-10 keV observed frame is represented as a black line. It is modelled with the BNTorus model (direct emission, blue dotted line) and an unabsorbed power law (scattering component, orange dotted-dashed line). The free parameters values of the model are $z = 2.309$, $N = 1.68 \times 10^{-4}$ and $N_{\rm H} = 10^{20}{\rm cm}^{-2}$ (left) and $N_{\rm H} = 1.5 \times 10^{24}{\rm cm}^{-2}$ (right).

The BNTorus is only defined for certain values of $N_{\rm H}$. The extrapolation between grid values done internally in XSPEC does not work correctly so we have used only those $N_{\rm H}$ values in the grid[9]. We have adopted the lowest value of $N_{\rm H}$ that produced a count rate below the observed upper limit.

For every AGN we usually have more than one observation and for every observation, we can have data from more than one EPIC camera (MOS and/or pn). So we run the code for every observation and camera. This way we end up with various $N_{\rm H}$ for every object. We select the most restrictive value of $N_{\rm H}$ (the highest) as the lower-limit. The final $N_{\rm H}$ obtained for the non-detected AGN are listed in Table 1.

4.2.2 AGN with low-quality spectra

We have 3 AGN – with sample IDs 66, 143 and 173 – with low-quality spectra ($n < 50$ counts). For these three AGN we have an absorbed luminosity derived from the observed flux, assuming a power-law continuum model with $\Gamma = 1.9$. As we have measurements of their count rate we can estimate their $N_{\rm H}$. To obtain

[9]The values of $\log_{10}(N_{\rm H})$ rounded to two decimal places are: [20.00, 20.15, 20.30 , 20.45, 20.60, 20.75, 20.90, 21.05, 21.20, 21.35, 21.50, 21.65, 21.80, 21.95, 22.10, 22.25, 22.40, 22.55, 22.70, 22.85, 23.00, 23.15, 23.30, 23.45, 23.60, 23.75, 23.90, 24.05, 24.20, 24.35, 24.50, 24.65, 24.80, 24.95, 25.10, 25.25, 25.40, 25.55, 25.70, 25.85, 26]

the normalization of the BNTorus model we follow the same procedure as before.

Once obtained the normalization, we increase the column density and we compare the observed 2-10 keV luminosity with the predicted observed luminosity of the model. We then adopt the $N_{\rm H}$ that predicted an observed luminosity equal or less than the one measured. The results for these AGN are shown in Table 1.

For AGN with identifier 143 our estimate of the X-ray column density is $\log_{10}(N_{\rm H}\ /{\rm cm}^{-2}) \geq 26$. In this case, even with the highest column density allowed by the model, we obtain always higher model luminosities than the observed ones. That is because at a certain column density all the direct X-ray emission is absorbed remaining only the scattering component, which does not change with increasing $N_{\rm H}$. Due to code implementation in these cases the maximum column density is assigned. According to Noguchi, Terashima & Awaki (2009) [55] some AGN could have a scattering component lower than 1%, reaching values as low as 0.5%. We have checked whether our AGN might belong to this population repeating the process with a scattering normalization of 0.5% the direct contribution normalization. The resulting luminosity of the scattering component is very similar to the one observed, a 37 % higher. Since it is unaffected by the obscuration, our column density estimate is the value that completely suppresses the AGN direct emission in the observed 2-10 keV range. So for this case we have a lower limit $\log_{10}(N_{\rm H}\ /{\rm cm}^{-2}) \geq 24.8$.

Most of the sample is absorbed (96% with $N_{\rm H} > 10^{22}$ cm^{-2}, or 22 AGN), i.e., the torus is blocking our line of sight. The only unabsorbed AGN (with sample ID 112) is highly off-axis. Consequently, it is possible that it was not detected only because of the low effective exposure time resultant, not because of a high obscuration. Even assuming the lower limit of $N_{\rm H}$ 26% (6) of our AGN are CT ($N_{\rm H} > 1.5 \times 10^{24}$ cm^{-2}) and 78% (18) of the sample are highly-absorbed AGN ($N_{\rm H} > 1.5 \times 10^{23.5}$ cm^{-2}).

4.3 Exposure time determination

In this section, the exposure times needed for the detection of our CT candidates will be estimated. First, we will determine them assuming that they are observed using XMM-*Newton* with the same conditions as in the original observations. Then, we will estimate them using *Athena*.

4.3.1 XMM-*Newton* exposure times

If we want to do a thorough study of our AGN properties and put tight constraints on their N_{H}, we need to detect them in X-rays. To determine whether current technology lets us study them we are going to determine the exposure time necessary to detect them with XMM-*Newton*. For XMM-*Newton* all values of count-rate will be in the band 0.5-12 keV.

We will use Equation 4 to determine the exposure times. We use the count rates predicted with the BNTorus model and our estimates of N_{H}. To estimate the count rates we use RMF and ARF files extracted at the position of the objects in the XMM-*Newton* field-of-view. This guarantees that we are simulating the real observing conditions: same relative position of the source, same PSF... With these assumptions, our simulations will return the expected count rate measured by XMM-*Newton*.

To estimate the background count rate we follow a similar procedure. Again we rely on the observations with XMM-*Newton*. We have the spectrum of the background for the deepest observation for every AGN. Unfortunately, it is not possible to directly load the background file into PyXspec and read the expected background count rate. To bypass this problem we load the source spectrum file of the observation. This way any prediction of the model will take into account the RMF, ARF and the corresponding background level. XSPEC directly gives us the total count rate (source plus background) and the net count rate (background corrected). Then our background count rate is just the difference between them.

To properly obtain the source count rate it is necessary to take into account the EEF and the scaling relation between background and source area. Fortunately, both effects are taken into account directly by PyXspec. The results are in Table 1.

4.3.2 Exposure times with *Athena*

Athena has two instruments, WFI and X-IFU. The one that will be most frequently used for surveys is WFI, and so, we are going to determine the detection time with the WFI. We need the same information – count rate of background and source – to estimate the exposure time needed with *Athena* to detect our sources. The RMF for the WFI has been obtained from the WFI webpage[10]. For all cases, we are using a field-of-view average RMF. As we are not assuming a certain

[10]In the `http://www.mpe.mpg.de/ATHENA-WFI/response_matrices.html` the file can be found

position of the source in the field-of-view, i.e. we do not require the sources to be the target of the observation, the situation is more similar to that in a survey.

Knowing the model and having the response matrix files obtaining the source count rate is trivial. Nonetheless, in this case, the EEF is not in the RMF and we have to correct the count rate obtained by it. The PSF of *Athena* can be approximated as a 2D Gaussian function with radial symmetry. Knowing that it is HEW $= 5''$ we can obtain the width σ of the Gaussian function as:

$$\int_o^{\mathrm{HEW}/2} PSF(r)\mathrm{d}r = \frac{1}{\sigma^2}\int_o^{\mathrm{HEW}/2} r \times e^{\frac{-r^2}{2\sigma^2}}\mathrm{d}r = 1/2 \rightarrow \sigma = \frac{HEW}{2\sqrt{2\times\log 2}} = 2.1233$$

Then using Equation 6 we can obtain the EEF for *Athena*. Both measures, source and background count rate, have been obtained using extraction areas with $R = 5''$, then EEF$(R = 5'') = 0.9375$. All count rates were corrected by this factor.

For the background noise, we have relied on the background simulated spectra obtained also from the WFI webpage. As before we are using a field-of-view average and we are taking into account both the photon and particle background. The area of background detection and source detection are the same, so in this case, the scale factor is 1. Standard full band *Athena* results are usually quoted in the 0.5-10 keV band and we do the same. The results are shown in Table 1.

We have done the simulations using the lower limit values of N_{H}. However, our objects might have absorption levels well above our computed values of N_{H}. Could *Athena* detect these objects if they are CT? To answer this question we have repeated our computations assuming that all sources are CT – $\log_{10}(N_{\mathrm{H}}\ /\ \mathrm{cm}^{-2}) = 24.2$ – and even the case of extreme X-ray obscuration – $\log_{10}(N_{\mathrm{H}}\ /\ \mathrm{cm}^{-2}) = 25.1$–. The results are summarized in Table 2.

AGN ID	z	Class	$t_{\text{Lower limit}}$ / ks	$t_{N_H=24.2}$ / ks	$t_{N_H=25.1}$ / ks
3	1.100	1	9.3	15.5	19.9
7	1.900	1	7.1	-	7.5
34	0.334	2	9.2	17.2	18.0
56	0.482	2	14.8	19.6	21.2
58	0.681	2	14.1	39.0	44.7
66	0.148	2	9.0	9.4	9.6
98	2.309	1	5.4	-	9.7
105	0.453	2	15.1	25.0	26.9
112	0.723	2	0.2	25.2	29.0
113	0.292	2	22.2	57.7	60.7
117	0.628	2	7.8	19.0	21.2
121	0.306	2	1.8	16.9	17.7
131	0.625	2	4.0	4.5	5.0
133	0.344	2	1.7	16.6	17.4
135	0.264	1	9.4	9.98	10.4
136	0.199	2	8.3	9.6	9.9
139	0.527	2	5.2	15.1	16.4
143	0.084	2	1.3	-	1.3
173	0.092	2	11.4	-	11.4
188	1.538	1	20.3	-	22.3
199	0.946	2	18.2	-	19.8
200	0.568	2	4.3	5.7	6.2
240	0.628	2	9.2	10.5	11.6

Table 2: Column 1: sample identifier of the AGN; column 2: redshift of the AGN; column 3: classification following the notation as Table 5; column 4: exposure time with *Athena* assuming $N_{\rm H}$ equal to the lower limit estimated in 4.2; column 5: exposure time with *Athena* assuming $\log_{10}(N_{\rm H}\ /\ {\rm cm}^{-2}) = 24.2$; column 6: exposure time with *Athena* assuming $\log_{10}(N_{\rm H}\ /\ {\rm cm}^{-2}) = 25.1$. For columns 4 and 5 if the estimated lower-limit of $N_{\rm H}$ is higher than $\log_{10}(N_{\rm H}\ /\ {\rm cm}^{-2}) = 24.2$ or $\log_{10}(N_{\rm H}\ /\ {\rm cm}^{-2}) = 25.1$ respectively no result is shown.

5. Discussion

Our study has allowed us to obtain several interesting results:

1. None of the empirical relations between mid-infrared and X-ray luminosities work for mid-infrared selected AGN. If we use these relations we would overestimate the X-ray luminosity of the AGN on average by 37.3% and 77.6% using the Stern (2015) [64] and the Chen et al. (2017) [65] relations, respectively. Consequently, we would have an overestimation of the $N_{\rm H}$ that would lead to a wrong classification of many AGN as Compton Thick. In our work, we have obtained a valid relation for mid-infrared selected AGN.

The different relationship between mid-infrared and X-ray luminosities found for mid-infrared and X-ray selected AGN can not be an effect of obscuration since the X-ray luminosities we are using are corrected by it. The effect must due to the nature of the AGN selection. As seen in Figure 12 there is always a certain dispersion between $L_{\rm X}$ and $L_{6\mu{\rm m}}$. At a fixed infrared luminosity, X-ray selected AGN samples preferentially to detect the brightest AGN in X-rays, while infrared-selected samples should be biased towards the infrared brightest AGN. Consequently, if we use the published relations in the literature we would be overestimating the X-ray luminosities of our WISE-selected sources.

To properly describe the relation between $L_{\rm X}$ and $L_{6\mu{\rm m}}$ we used a lineal empirical fit of the form $\log_{10}(L_{\rm X}) = m \times \log_{10}(L_{6\ \mu m}) + b$. Using the least squares method we obtain the best linear fit as $m = 0.854$ and $b = 7.952$. This relation is expected to describe better mid-infrared selected AGN samples than traditional ones (Stern (2015) [64] or Chen et al. (2017) [65]).

2. We have also estimated $N_{\rm H}$ for the Compton-Thick candidates. We can see a histogram of all the values in Figure 15. Almost all our sample objects are absorbed (96% with $N_{\rm H} > 10^{22}$ cm^{-2}; 22 AGN), i.e., the torus is blocking our line of sight. There is an object without $N_{\rm H}$ estimation (with sample ID 112) because is highly off-axis. We need deeper observations to reveal the true nature of the object.

Furthermore, based on our $N_{\rm H}$ estimates 26% (6) of the CT candidates are actually CT ($N_{\rm H} > 1.5 \times 10^{24}$ cm^{-2}) and 78% (18) are highly-absorbed AGN ($\log_{10}(N_{\rm H}\ /{\rm cm}^{-2}) \geq 23.5$). Our sample is not only detecting obscured AGN but highly to extremely obscured AGN. Most of our $N_{\rm H}$ are so close to the CT limit

that there is a high chance that most sample sources are indeed CT AGN. If we take into account just those confirmed as AGN 38% (5) of the CT candidates are CT and every one is absorbed.

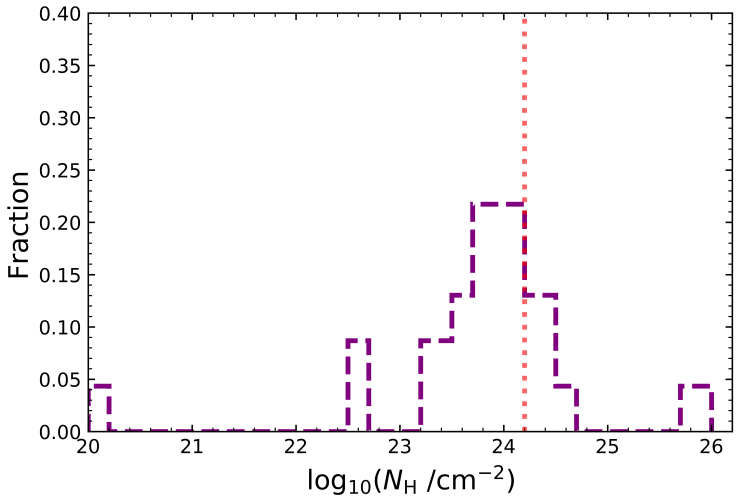

Figure 15: Column density distribution for CT candidates. The red dotted line indicates the CT limit $\log_{10}(N_{\rm H}\ /\ {\rm cm}^{-2}) = 24.2$.

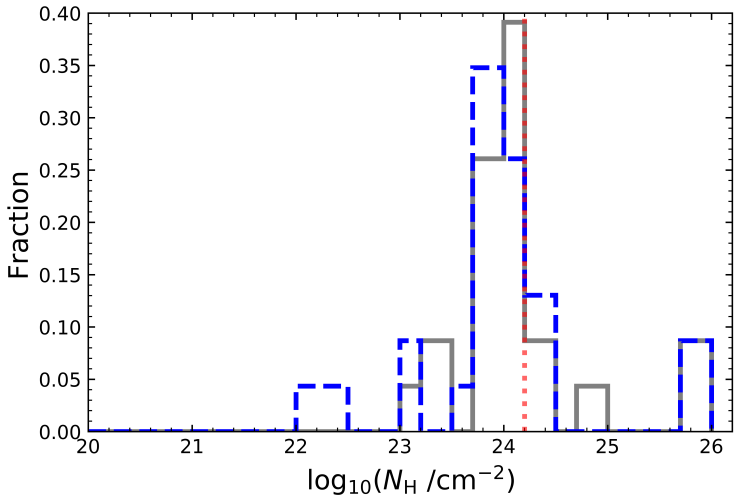

Figure 16: Column density distribution for CT candidates using Stern – blue dashed line – and Chen – grey solid line – relations. The red dotted line indicates the CT limit $\log_{10}(N_{\rm H}\ /\ {\rm cm}^{-2}) = 24.2$.

All of our type 1 CT candidates are heavily absorbed (5 objects) and even 2 of them are CT AGN. This is an unexpected result as type 1 AGN are not expected to be obscured ($N_{\rm H} = 10^{22}$ cm^{-2}) and the X-ray column densities found for these objects are typically $< 10^{23}$ cm^{-2} [66, 67]. These results are telling us that X-ray surveys are not only losing highly absorbed type 2 AGN but also highly absorbed type 1 AGN.

We have shown that Stern (2015) [64] and Chen et al. (2017) [65] relations lead to an important overestimation of the intrinsic X-ray luminosity for our sources. If this error would be propagated to the determination of $N_{\rm H}$ we would have an median overestimation for $N_{\rm H}$ of 41.2% for the Chen et al. (2017) [65] relation and 41.1% for the Stern (2015) [64] relation. The results of these new simulations are in figure 3 and in Figure 16. This would have increased the number of CT AGN by 2 using the Stern (2015) [64] relation (from 26% to 35%) and by 5 using the Chen et al. (2017) [65] relation (from 26% to 48%).

Considering the full WISE sample, the fraction of obscured AGN is 58%. This demonstrates that the infrared selection is a reliable way to detect highly obscured AGN, although restricted to luminous objects. Even more, with an infrared selection, a 7% of the sample is CT. The fraction would vary from 6% to 11% depending on whether we consider all 5 sources without redshift as CT or not.These AGN would be lost in an X-ray selection at the depths that can be achieved with current instrumentation, leading to a systematic bias against the most highly obscured AGN.

AGN ID	**z**	**Class**	$\mathbf{N_H}$ / $\mathbf{cm^{-2}}$	$\mathbf{N_{H\ Stern}}$ / $\mathbf{cm^{-2}}$	$\mathbf{N_{H\ Chen}}$ / $\mathbf{cm^{-2}}$
3	1.100	1	23.90	23.90	24.05
7	1.900	1	24.65	24.35	24.50
34	0.334	2	23.60	23.75	23.90
56	0.482	2	23.90	24.05	24.20
58	0.681	2	23.60	24.05	24.20
66	0.148	2	24.05	23.75	23.90
98	2.309	1	24.20	23.90	24.05
105	0.453	2	23.75	23.90	23.90
112	0.723	2	20.00	22.25	23.14
113	0.292	2	23.45	23.75	23.75
117	0.628	2	23.60	23.75	23.90
121	0.306	2	22.70	23.15	23.30
131	0.625	2	24.05	24.05	24.20
133	0.344	2	22.70	23.15	23.30
135	0.264	1	24.05	24.20	24.20
136	0.199	2	23.90	24.05	24.05
139	0.527	2	23.45	23.60	23.75
143	0.084	2	24.65	26.00	26.00
173	0.092	2	24.50	26.00	26.00
188	1.538	1	24.50	24.35	24.50
199	0.946	2	24.35	24.50	24.80
200	0.568	2	23.90	23.90	24.05
240	0.628	2	24.05	24.05	24.20

Table 3: Column 1: sample identifier of the AGN; column 2: redshift of the AGN; column 3: column density obtained using our own empirical relation between L_X and $L_{6\mu m}$; column 4: column density obtained using the Stern (2015) [64] relation; column 5: column density obtained using the Chen et al. (2017) [65] relation.

3. Although infrared selected samples allow selecting candidates to highly obscured AGN, we need deep X-ray observations to study their properties and identify how many objects are highly obscured and how many are CT AGN. We have estimated the minimum exposure time required to detect our AGN with XMM-*Newton*. The necessary observation time for detection with SNR = 5 is too long, all of them needing more than 100ks. Furthermore, 5 AGN (22% of the CT candidates) would require more than 1 Ms just to be detected.

To contextualize the results we can compare our exposure times with the distribution of exposure times used in the observations included in the 3XMM-DR8 catalogue. Figure 17 shows these distributions. It can be seen that almost no observation is longer than 100ks while our lowest estimated time is slightly over 90ks. There is just one case with a reasonable exposure time, the AGN with ID 112. Because it is highly off-axis it have not N_{H} estimation, consequently estimated time is not reliable. So, even assuming we would be granted with time to make observations comparable in depth to the deepest ones carried out so far with XMM-*Newton* (100-150 ks) we would be able to detect only 2 AGN of our sample, disregarding AGN 112.

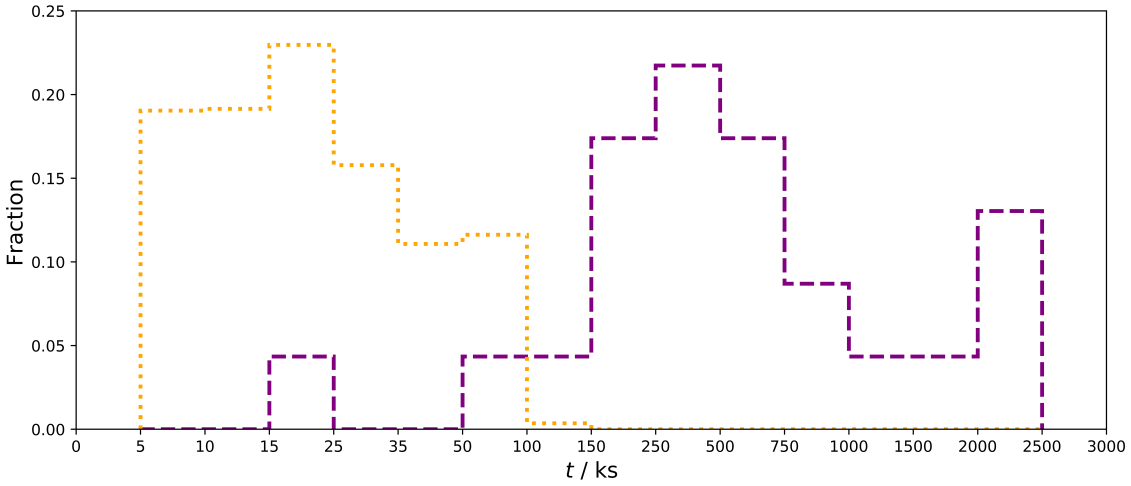

Figure 17: Dashed purple line: distribution of exposure times needed to detect with SNR = 5 our AGN with XMM-*Newton*; orange dotted line: observation times with XMM-*Newton* from 3XMM catalogue. Times are estimated assuming the use of the same camera as the one from the deepest observation. The bin scale is not lineal to allow a proper representation of results.

But even worse, these times are lower-limits to the exposure time that would be needed to detect them, since the obscuration could be substantially higher than our current estimates. Also, these times are just for detection but to obtain a high-quality spectrum – which allow through its fit to recover parameters such as $N_{\rm H}$ – we would need much more time. So neither XMM-*Newton* nor Chandra are feasible options to study these AGN in the X-ray band.

To detect all objects in a reasonable exposure time we would have to wait for the next generation of X-ray observatories. We have repeated our simulations but taking now the future capabilities of the WFI instrument onboard the *Athena* observatory. The results, presented in Table 1, show that with short exposures ($t < 25$ ks) we can detect all objects with SNR$=5$ if their $N_{\rm H}$ coincide with our estimates. In Figure 18 we can see the comparison between XMM-*Newton* and *Athena* exposure times. The improvement is huge, even the most time-consuming AGN with *Athena* ($t \approx 22.2$ ks) is well below from the lowest exposure time that would be required with XMM-*Newton* ($t \approx 93.6$ ks) and approximately 70% of the sample could be detected in very short exposures of less than 10ks.

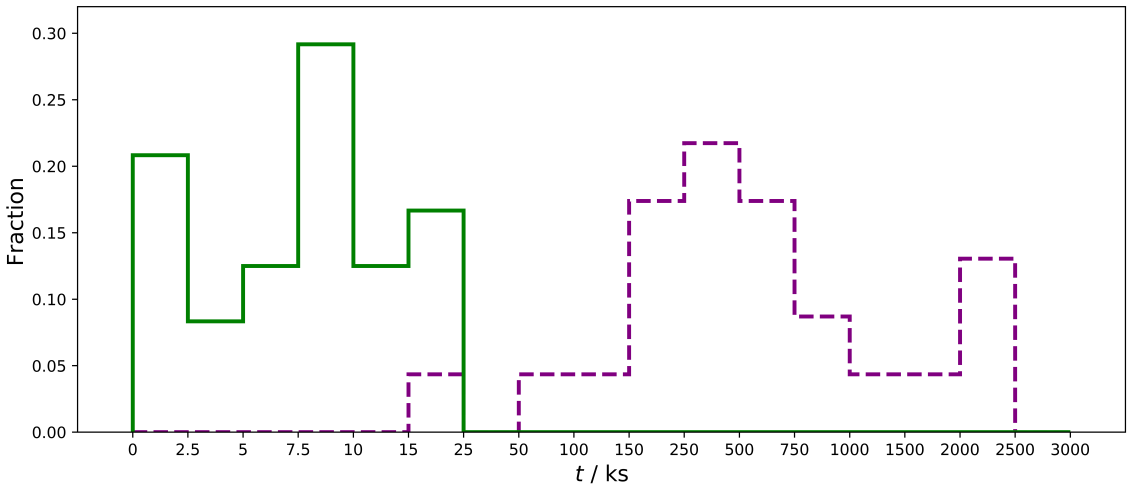

Figure 18: Distribution of exposure times with *Athena* (green solid line) and XMM-*Newton* (purple dashed line). The bin scale is not lineal to allow a proper representation.

Our estimations of $N_{\rm H}$ are a lower limit so the obscuration could be substantially higher. We have repeated our simulations assuming all our AGN were at the CT limit, $\log_{10}(N_{\rm H}\ /\ {\rm cm}^{-2}) = 24.2$, or even extremely absorbed, $\log_{10}(N_{\rm H}\ /\ {\rm cm}^{-2}) = 25.1$. The results are in Table 2 and represented in Figure 19.

Although the exposure times have increased, the numbers are still reasonable and achievable with *Athena*. For $\log_{10}(N_{\rm H}\ /\ {\rm cm}^{-2}) = 25.1$ the exposure times are still below 58 ks while for $\log_{10}(N_{\rm H}\ /\ {\rm cm}^{-2}) = 24.2$ they are below 61 ks. Furthermore, for both cases, 91% of the sample would be detected with exposure times lower than 30 ks.

As introduced in Section 2.2.2 the WFI will be used by *Athena* to make several surveys with different depths. The shallowest survey will have an exposure time of 86 ks which is far more than the exposure time needed to detect our AGN. So *Athena* will detect routinely highly obscured sources such as ours. With this new population within our reach, a new window to study the formation and evolution of galaxies will be open. *Athena* is expected to survey around 42.5 deg^2 with a deep of $t_{\rm obs} = 86$ ks while the WISE sample covers around 6 deg^2. Consequently according to our results we can expect to detect with *Athena* at least 7 more times CT to a total of 42 CT AGN.

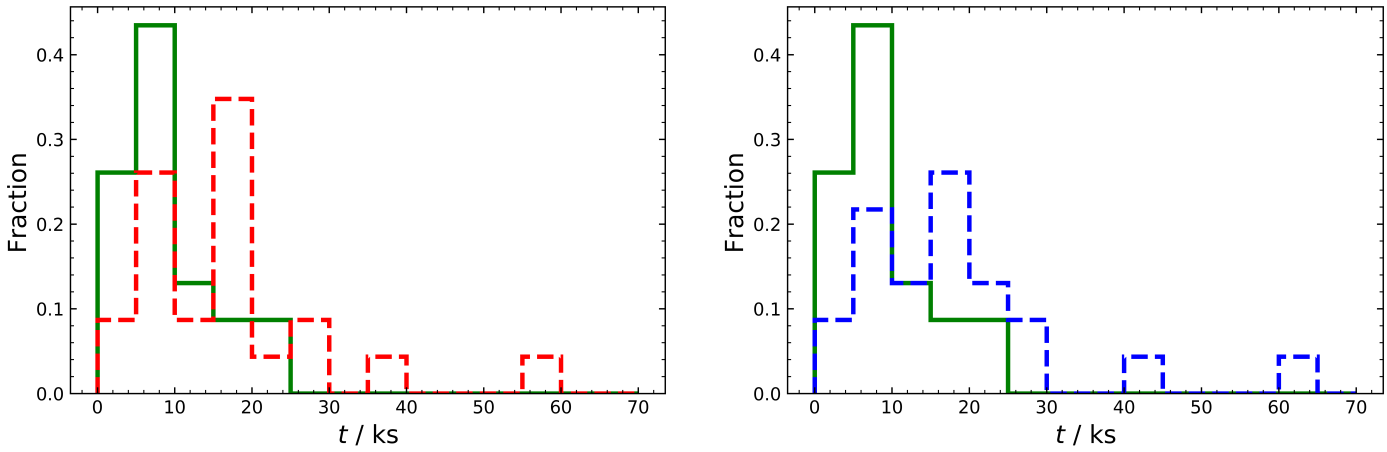

Figure 19: Exposure time needed to detect with SNR = 5 our AGN with *Athena* assuming $\log_{10}(N_{\rm H}\ /\ {\rm cm}^{-2}) = 24.2$ (left, red dashed line) and $\log_{10}(N_{\rm H}\ /\ {\rm cm}^{-2}) = 25.1+$ (right, blue dashed line) versus exposure time estimations for our lower limits of $N_{\rm H}$ (solid green line). If the original lower-limit of $N_{\rm H}$ is higher than the value of the corresponding case we use the former.

We can use our results to estimate the total expected counts detected in the 0.5-12 keV energy band in the shallowest survey with the WFI. To do that we just multiply the count rate of the model by the exposure time of the survey, $t = 86$ ks. The results are summarized in Table 4. For 4 AGN (17%) we will be able to obtain

good quality spectrum – more than 1000 net counts from the source (background subtracted) – and for the rest of the sample, the spectra will have sufficient counts (>100 net counts) to put tight constraints to their $N_{\rm H}$.

AGN ID	**z**	**Class**	$\mathbf{N_H}$ / $\mathbf{cm^{-2}}$	m /counts s^{-1}	Total counts
3	1.100	1	23.90	0.00349	300
7	1.900	1	24.65	0.00440	379
34	0.334	2	23.60	0.00352	302
56	0.482	2	23.90	0.00237	203
58	0.681	2	23.60	0.00246	211
66	0.148	2	24.05	0.00357	307
98	2.309	1	24.20	0.00559	480
105	0.453	2	23.75	0.00233	201
112	0.723	2	20.00	0.11948	10275
113	0.292	2	23.45	0.00172	148
117	0.628	2	23.60	0.00407	350
121	0.306	2	22.70	0.01538	1323
131	0.625	2	24.05	0.00729	627
133	0.344	2	23.90	0.01644	1414
135	0.264	1	23.45	0.00345	296
136	0.199	2	26.00	0.00382	328
139	0.527	2	24.50	0.00580	499
143	0.084	2	26.00	0.02120	1823
173	0.092	2	24.50	0.00294	253
188	1.538	1	24.50	0.00184	158
199	0.946	2	24.35	0.00201	172
200	0.568	2	23.90	0.00694	597
240	0.628	2	24.05	0.00351	301

Table 4: Column 1: sample identifier of the AGN; column 2: redshift of the AGN; column 3: classification following the same notation as Table 5; column 4: lower-limit for the column density in logarithmic units (see Section 4.2); column 5: count rate of the AGN from our simulations; column 6: total counts estimated from our simulations for an exposure time of $t = 86$ ks.

6. Conclusions

The study of obscured AGN is fundamental to fully understand galaxy formation and evolution. Traditionally X-ray surveys have lost the most obscured AGN – the so-called Compton Thick – but mid-infrared selected samples allow to obtain an unbiased sample of both obscured and unobscured AGN. In this work, we have a unique sample of mid-infrared selected AGN with deep X-ray measures.

We have first checked that the relations between X-ray and mid-infrared luminosities do not describe correctly a mid-infrared selected sample. After that, we obtain our own relation that describes properly mid-infrared selected AGN relation between X-ray and mid-infrared luminosities. Applying it we had been able to obtain an estimation of the intrinsic X-ray luminosity for a sample of CT candidates: undetected AGN at X-rays and AGN with low-quality X-ray spectra. Using these estimated intrinsic X-ray luminosities and measures or upper-limit of the emission we estimated a lower limit for the CT candidates obscuration. Then we estimated that exposure times needed to detect them with XMM-*Newton* are unfeasible but exposure time estimated to detect them with *Athena* are reasonable. From the results we can conclude that:

- Mid-infrared selected AGN are X-ray weak in comparison with those selected in the X-ray range. This difference must be taken into account to avoid an overestimation in X-ray luminosity of mid-infrared selected AGN. Otherwise, it would lead to an overestimation of the obscuration estimated and consequently the fraction of CT AGN derived would be overestimated.
- Using mid-infrared selected AGN samples we can detect CT AGN, revealing an undetected population of AGN in X-rays. Some AGN of this population are type 1 AGN.
- Detecting and thoroughly studying these AGN is not possible with current X-ray observatories such as XMM-*Newton*. *Athena* will detect them routinely during the planned survey opening the opportunity to finally detect and study in detail the most obscured AGN.

References

[1] J. Kormendy and D. Richstone, "Inward Bound—The Search For Supermassive Black Holes In Galactic Nuclei," *Annual Review of Astronomy and Astrophysics*, vol. 33, p. 581, 1995.

[2] J. Kormendy, "Supermassive Black Holes in Galactic Nuclei," in *Revista Mexicana de Astronomia y Astrofisica Conference Series*, J. Cantó and L. F. Rodríguez, Eds., vol. 10, Mar 2001, pp. 69–78.

[3] K. Gebhardt, R. Bender, G. Bower, and others., "A Relationship between Nuclear Black Hole Mass and Galaxy Velocity Dispersion," *The Astrophysical Journal*, vol. 539, pp. L13–L16, Aug. 2000.

[4] K. Gültekin, D. Richstone, K. Gebhardt, and others., "The M-σ and M-L Relations in Galactic Bulges, and Determinations of Their Intrinsic Scatter," *The Astrophysical Journal*, vol. 698, pp. 198–221, Jun. 2009.

[5] L. Ferrarese and D. Merritt, "A Fundamental Relation between Supermassive Black Holes and Their Host Galaxies," *The Astrophysical Journal*, vol. 539, pp. L9–L12, Aug. 2000.

[6] P. Madau and M. Dickinson, "Cosmic Star-Formation History," *Annual Review of Astronomy and Astrophysics*, vol. 52, pp. 415–486, Aug 2014.

[7] W. N. Brandt and D. M. Alexander, "Cosmic X-ray surveys of distant active galaxies. The demographics, physics, and ecology of growing supermassive black holes," *Astronomy and Astrophysics Review*, vol. 23, p. 1, Jan 2015.

[8] D. Rigopoulou, V. Mainieri, O. Almaini *et al.*, "Spectral energy distributions of type 2 quasi-stellar objects: obscured star formation at high redshifts," *Monthly Notices of the Royal Astronomical Society*, vol. 400, pp. 1199–1207, Dec. 2009.

[9] E. Treister, P. Natarajan, D. B. Sand ers *et al.*, "Major Galaxy Mergers and the Growth of Supermassive Black Holes in Quasars," *Science*, vol. 328, no. 5978, p. 600, Apr 2010.

[10] Swinburne University of Technology. Cosmos: Column density. [Online]. Available: http://astronomy.swin.edu.au/cosmos/C/Column+Density

[11] A. Merloni, A. Bongiorno, M. Brusa *et al.*, "The incidence of obscuration in active galactic nuclei," *Monthly Notices of the Royal Astronomical Society*, vol. 437, no. 4, pp. 3550–3567, Feb 2014.

[12] A. Comastri, "Compton-Thick AGN: The Dark Side of the X-Ray Background," in *Supermassive Black Holes in the Distant Universe*, ser. Astrophysics and Space Science Library, A. J. Barger, Ed., vol. 308, 2004, p. 245.

[13] R. C. Hickox and D. M. Alexander, "Obscured Active Galactic Nuclei," *Annual Review of Astronomy and Astrophysics*, vol. 56, pp. 625–671, Sep 2018.

[14] P. Padovani, D. M. Alexander, R. J. Assef *et al.*, "Active galactic nuclei: what's in a name?" *The Astronomy and Astrophysics Review*, vol. 25, no. 1, p. 2, Aug 2017.

[15] P. Jovanović and L. Č. Popović, "X-ray Emission From Accretion Disks of AGN: Signatures of Supermassive Black Holes," *arXiv e-prints*, p. arXiv:0903.0978, Mar 2009.

[16] K. I. Kellermann, R. Sramek, M. Schmidt *et al.*, "VLA observations of objects in the Palomar Bright Quasar Survey," *Astronomical Journal*, vol. 98, pp. 1195–1207, Oct. 1989.

[17] L. Spinoglio and M. A. Malkan, "Infrared line diagnostics of active galactic nuclei," *The Astrophysical Journal*, vol. 399, pp. 504–520, Nov. 1992.

[18] R. Siebenmorgen, M. Haas, E. Pantin, E. Krügel, C. Leipski, H. U. Käufl, P. O. Lagage, A. Moorwood, A. Smette, and M. Sterzik, "Nuclear activity in nearby galaxies. Mid-infrared imaging with the VLT," *Astronomy and Astrophysics*, vol. 488, pp. 83–90, Sep. 2008.

[19] D. Stern, P. Eisenhardt, V. Gorjian *et al.*, "Mid-Infrared Selection of Active Galaxies," *The Astrophysical Journal*, vol. 631, pp. 163–168, Sep. 2005.

[20] A. Alonso-Herrero, P. G. Pérez-González, D. M. Alexander, and other, "Infrared Power-Law Galaxies in the Chandra Deep Field-South: Active Galactic Nuclei and Ultraluminous Infrared Galaxies," *The Astrophysical Journal*, vol. 640, pp. 167–184, Mar. 2006.

[21] S. Mateos, A. Alonso-Herrero, F. J. Carrera *et al.*, "Using the Bright Ultrahard XMM-Newton survey to define an IR selection of luminous AGN based on WISE colours," *Monthly Notices of the Royal Astronomical Society*, vol. 426, pp. 3271–3281, Nov. 2012.

[22] R. J. Assef, D. Stern, C. S. Kochanek *et al.*, "Mid-infrared Selection of Active Galactic Nuclei with the Wide-field Infrared Survey Explorer. II. Properties of WISE-selected Active Galactic Nuclei in the NDWFS Boötes Field," *The Astrophysical Journal*, vol. 772, p. 26, Jul. 2013.

[23] E. L. Wright, P. R. M. Eisenhardt, A. K. Mainzer *et al.*, "The Wide-field Infrared Survey Explorer (WISE): Mission Description and Initial On-orbit Performance," *Astronomical Journal*, vol. 140, pp. 1868–1881, Dec. 2010.

[24] X. Barcons, F. J. Carrera, M. G. Watson *et al.*, "The XMM-Newton serendipitous survey . II. First results from the AXIS high galactic latitude medium sensitivity survey," *Astronomy and Astrophysics*, vol. 382, pp. 522–536, Feb 2002.

[25] S. Bianchi and M. Guainazzi, "The nature of the soft X-ray emission in obscured AGN," in *The Multicolored Landscape of Compact Objects and Their Explosive Origins*, ser. American Institute of Physics Conference Series, T. di Salvo, G. L. Israel, L. Piersant, L. Burderi, G. Matt, A. Tornambe, and M. T. Menna, Eds., vol. 924, Aug 2007, pp. 822–829.

[26] NASA, JPL, and Caltech. (2013) The Wide-field Infrared Survey Explorer All-Sky Data Release. [Online]. Available: http://wise2.ipac.caltech.edu/docs/release/allsky/

[27] ESA. The european photon imaging camera (epic) onboard xmm-newton. [Online]. Available: https://www.cosmos.esa.int/web/xmm-newton/technical-details-epic

[28] L. Strüder, U. Briel, K. Dennerl *et al.*, "The European Photon Imaging Camera on XMM-Newton: The pn-CCD camera," *Astronomy and Astrophysics*, vol. 365, pp. L18–L26, Jan. 2001.

[29] ESA. XMM-Newton Survey Science Centre. [Online]. Available: http://xmmssc.irap.omp.eu/

[30] S. R. Rosen, N. A. Webb, M. G. Watson *et al.*, "The XMM-Newton serendipitous survey. VII. The third XMM-Newton serendipitous source catalogue," *Astronomy and Astrophysics*, vol. 590, p. A1, May 2016.

[31] M. G. Watson, A. C. Schröder, D. Fyfe *et al.*, "The XMM-Newton serendipitous survey. V. The Second XMM-Newton serendipitous source catalogue," *Astronomy and Astrophysics*, vol. 493, pp. 339–373, Jan. 2009.

[32] XMM-Newton Science Operations Centre. Off-axis effective area. [Online]. Available: https://xmm-tools.cosmos.esa.int/external/xmm_user_support/documentation/uhb/effareaoffaxis.html

[33] ESA. Athena: Mission summary. [Online]. Available: http://sci.esa.int/athena/59896-mission-summary/

[34] Oficina de la Comunidad de Athena. La misión Athena. [Online]. Available: https://www.the-athena-x-ray-observatory.eu/es/mission-2.html

[35] The X-IFU consortium. X-IFU in a nutshell. [Online]. Available: http://x-ifu.irap.omp.eu/the-x-ifu-in-a-nutshell/

[36] ESA. XMM-Newton Users Handbook. [Online]. Available: https://xmm-tools.cosmos.esa.int/external/xmm_user_support/documentation/uhb/basics.html

[37] Max Planck Institüt. Wide Field Imager Overview. [Online]. Available: http://www.mpe.mpg.de/ATHENA-WFI/

[38] Chandra X-Ray Center. Acis instrument information. [Online]. Available: http://cxc.harvard.edu/cal/Acis/

[39] S. Mateos, F. J. Carrera, A. Alonso-Herrero *et al.*, "X-Ray Absorption, Nuclear Infrared Emission, and Dust Covering Factors of AGNs: Testing Unification Schemes," *The Astrophysical Journal*, vol. 819, p. 166, Mar. 2016.

[40] A. Alonso-Herrero, C. Ramos Almeida, R. Mason, A. Asensio Ramos, P. F. Roche, N. A. Levenson, M. Elitzur, C. Packham, J. M. Rodríguez Espinosa, S. Young, T. Díaz-Santos, and A. M. Pérez-García, "Torus and Active Galactic Nucleus Properties of Nearby Seyfert Galaxies: Results from Fitting Infrared Spectral Energy Distributions and Spectroscopy," *The Astrophysical Journal*, vol. 736, no. 2, p. 82, Aug 2011.

[41] A. Kirkpatrick, A. Pope, D. M. Alexander *et al.*, "GOODS-Herschel: Impact of Active Galactic Nuclei and Star Formation Activity on Infrared Spectral Energy Distributions at High Redshift," *The Astrophysical Journal*, vol. 759, no. 2, p. 139, Nov 2012.

[42] M. J. I. Brown, K. J. Duncan, H. Landt, M. Kirk, C. Ricci, N. Kamraj, M. Salvato, and T. Ananna, "The Spectral Energy Distributions of Active Galactic Nuclei," *arXiv e-prints*, Aug. 2019.

[43] K. A. Arnaud, "XSPEC: The First Ten Years," in *Astronomical Data Analysis Software and Systems V*, ser. Astronomical Society of the Pacific Conference Series, G. H. Jacoby and J. Barnes, Eds., vol. 101, 1996, p. 17.

[44] E. Torresi and G. Lanzuisi. Chandra tutorial. [Online]. Available: http://labx.iasfbo.inaf.it/2014/resources/chandra_tut.pdf

[45] Chandra X-Ray Center. Rmf: Redistribution matrix file. [Online]. Available: http://cxc.harvard.edu/ciao/dictionary/rmf.html

[46] K. D. Murphy and T. Yaqoob, "An X-ray spectral model for Compton-thick toroidal reprocessors," *Monthly Notices of the Royal Astronomical Society*, vol. 397, pp. 1549–1562, Aug. 2009.

[47] M. Baloković, M. Brightman, F. A. Harrison *et al.*, "New Spectral Model for Constraining Torus Covering Factors from Broadband X-Ray Spectra of Active Galactic Nuclei," *The Astrophysical Journal*, vol. 854, no. 1, p. 42, Feb 2018.

[48] M. Brightman and K. Nandra, "An XMM-Newton spectral survey of 12 μm selected galaxies - I. X-ray data," *Monthly Notices of the Royal Astronomical Society*, vol. 413, pp. 1206–1235, May 2011.

[49] Z. Liu, A. Merloni, A. Georgakakis *et al.*, "X-ray spectral properties of the AGN sample in the northern XMM-XXL field," *Monthly Notices of the Royal Astronomical Society*, vol. 459, pp. 1602–1625, Jun. 2016.

[50] A. Annuar, D. M. Alexander, P. Gandhi *et al.*, "A New Compton-thick AGN in our Cosmic Backyard: Unveiling the Buried Nucleus in NGC 1448 with NuSTAR," *The Astrophysical Journal*, vol. 836, p. 165, Feb. 2017.

[51] M. Guainazzi, G. Risaliti, H. Awaki *et al.*, "The nature of the torus in the heavily obscured AGN Markarian 3: an X-ray study," *Monthly Notices of the Royal Astronomical Society*, vol. 460, pp. 1954–1969, Aug. 2016.

[52] J. N. Reeves and M. J. L. Turner, "X-ray spectra of a large sample of quasars with ASCA," *Monthly Notices of the Royal Astronomical Society*, vol. 316, no. 2, pp. 234–248, Aug 2000.

[53] A. Corral, R. Della Ceca, A. Caccianiga *et al.*, "The X-ray spectral properties of the AGN population in the XMM-Newton bright serendipitous survey," *Astronomy and Astrophysics*, vol. 530, p. A42, Jun 2011.

[54] S. Mateos, X. Barcons, F. J. Carrera, and other, "X-ray spectra of XMM-Newton serendipitous medium flux sources," *Astronomy and Astrophysics*, vol. 433, no. 3, pp. 855–873, Apr 2005.

[55] K. Noguchi, Y. Terashima, and H. Awaki, "A New Sample of Buried Active Galactic Nuclei Selected from the Second XMM-Newton Serendipitous Source Catalogue," *The Astrophysical Journal*, vol. 705, no. 1, pp. 454–467, Nov 2009.

[56] O. Hainaut. Signal, noise and detection. [Online]. Available: http://www.eso.org/~ohainaut/ccd/sn.html

[57] R. O'Connell. Point spread functions. [Online]. Available: http://web.ipac.caltech.edu/staff/fmasci/home/astro_refs/PSFtheory.pdf

[58] XMM-Newton SOC/SSC . Encircled energy function. [Online]. Available: https://xmm-tools.cosmos.esa.int/external/sas/current/doc/eupper/node4.html

[59] A. M. Read, S. R. Rosen, R. D. Saxton, and J. Ramirez, "A new comprehensive 2D model of the point spread functions of the XMM-Newton EPIC telescopes: spurious source suppression and improved positional accuracy," *Astronomy and Astrophysics*, vol. 534, p. A34, Oct. 2011.

[60] D. Lutz, R. Maiolino, H. W. W. Spoon, and A. F. M. Moorwood, "The relation between AGN hard X-ray emission and mid-infrared continuum from ISO spectra: Scatter and unification aspects," *Astronomy and Astrophysics*, vol. 418, pp. 465–473, May 2004.

[61] P. Gandhi, H. Horst, A. Smette *et al.*, "Resolving the mid-infrared cores of local Seyferts," *Astronomy and Astrophysics*, vol. 502, pp. 457–472, Aug. 2009.

[62] D. Asmus, P. Gandhi, S. F. Hönig, A. Smette, and W. J. Duschl, "The subarcsecond mid-infrared view of local active galactic nuclei - II. The mid-infrared-X-ray correlation," *Monthly Notices of the Royal Astronomical Society*, vol. 454, pp. 766–803, Nov. 2015.

[63] S. Mateos, F. J. Carrera, A. Alonso-Herrero *et al.*, "Revisiting the relationship between 6 μm and 2-10 keV continuum luminosities of AGN," *Monthly Notices of the Royal Astronomical Society*, vol. 449, pp. 1422–1440, May 2015.

[64] D. Stern, "The X-Ray to Mid-infrared Relation of AGNs at High Luminosity," *The Astrophysical Journal*, vol. 807, p. 129, Jul. 2015.

[65] C.-T. J. Chen, R. C. Hickox, A. D. Goulding *et al.*, "The X-Ray and Mid-infrared Luminosities in Luminous Type 1 Quasars," *The Astrophysical Journal*, vol. 837, p. 145, Mar. 2017.

[66] S. Mateos, F. J. Carrera, M. J. Page *et al.*, "The XMM-Newton Wide Angle Survey (XWAS): the X-ray spectrum of type-1 AGN," *Astronomy and Astrophysics*, vol. 510, p. A35, Feb. 2010.

[67] A. Corral, M. J. Page, F. J. Carrera *et al.*, "Average Fe Kα emission from distant AGN," *Astronomy and Astrophysics*, vol. 492, pp. 71–80, Dec. 2008.

A. Summary table of the 96 AGN candidates

WISE ID	Sample ID	Confirmed	z	Class	$L_{6\mu m}$ / erg s^{-1}	$L_{6\mu m_{AGN}}$ / erg s^{-1}	L_X / erg s^{-1}
J130552.64+175203.0	3	1	1.1000	1	45.274	45.204	-
J130955.66+321122.7	5	1	0.3800	2	44.144	43.994	43.326
J131048.44+322253.4	7	1	1.9000	1	46.230	46.250	-
J124325.16+112442.6	9	1	-	-	-	-	-
J083252.81+525637.8	24	1	0.7887	1	45.638	45.436	43.830
J140944.08+261220.0	32	1	1.2620	1	45.669	45.569	43.936
J221824.30+001805.5	34	1	0.3340	2	44.105	43.785	-
J221813.91+001625.2	35	1	0.3326	2	43.933	43.462	43.839
J221723.69+001652.3	36	1	0.3004	2	44.027	43.625	43.153
J133417.53+375722.3	46	1	1.1433	1	45.420	45.236	44.437
J124429.36-003418.1	53	1	0.8276	1	45.067	43.886	44.310
J124555.11-003735.4	54	1	1.0409	1	45.419	44.750	44.796
J124540.99-002744.8	55	1	1.6866	1	45.763	45.804	45.341
J124544.41-001952.7	56	1	0.4820	2	44.257	44.168	-
J123816.14+620207.6	57	1	1.0006	1	45.206	44.355	43.913
J123718.55+620317.6	58	0	0.6810	2	44.777	44.299	-
J123716.02+620323.3	59	1	2.0591	1	45.910	46.009	43.986
J123759.57+621102.4	60	1	0.9084	1	45.144	43.796	44.621
J123800.95+621335.8	61	1	0.4400	1	44.555	43.969	43.494
J121400.37+140215.1	64	1	1.8420	1	45.836	45.960	44.266
J121356.19+140431.3	65	1	0.1543	1	43.709	43.513	43.439
J121405.67+140937.4	66	1	0.1480	2	43.451	43.091	42.283
J121448.56+135929.4	69	1	0.8070	1	44.873	44.440	43.655
J121509.46+135449.8	70	1	0.8461	1	45.401	44.810	44.619
J141642.42+521812.6	76	1	1.2819	1	46.110	46.002	44.461
J141741.87+522823.2	84	1	1.1482	2	45.695	45.516	44.209
J104401.13+212804.0	88	1	1.4950	1	46.200	46.098	44.834
J104505.22+212749.0	89	1	0.7463	1	45.192	44.496	44.052
J104522.14+212615.0	90	1	0.8912	1	45.434	45.115	44.603

WISE ID	Sample ID	Confirmed	z	Class	$L_{6\mu m}$ / erg s^{-1}	$L_{6\mu m_{AGN}}$ / erg s^{-1}	L_X / erg s^{-1}
J104351.61+213703.6	91	1	0.7210	1	44.987	44.156	43.568
J122549.13+332621.6	93	1	0.7040	2	45.018	44.751	43.524
J134748.61+173442.5	97	1	1.4719	1	46.197	46.162	44.482
J134754.70+173705.7	98	1	2.309	1	46.246	46.314	-
J105200.29+571805.5	101	1	1.1380	2	45.327	45.223	44.353
J105239.59+572431.4	102	1	1.1116	1	45.328	44.927	44.744
J105231.50+571752.1	104	1	0.7800	2	45.034	44.980	43.236
J103053.92+053311.7	105	0	0.4530	2	44.071	43.993	-
J103102.39+052329.8	106	1	-	-	-	-	-
J131110.23+280102.8	109	1	0.6810	2	44.876	44.536	44.047
J131234.66+275345.9	110	1	2.1500	1	46.169	46.035	44.742
J131246.83+275219.9	111	1	0.8660	1	45.099	44.127	44.700
J131304.96+275604.8	112	0	0.7230	2	44.716	44.541	-
J092043.97+370011.6	113	0	0.2920	2	43.742	43.143	-
J092155.70+371128.7	117	0	0.6280	2	44.766	44.494	-
J092129.17+370101.6	118	1	0.2426	1	43.739	43.476	43.402
J091951.82+370252.5	119	1	0.5330	2	44.493	44.265	43.628
J104155.73+061256.3	120	1	1.4731	1	45.640	45.474	44.117
J104204.59+060326.4	121	1	0.3060	2	44.293	43.686	-
J120308.89+442413.9	123	1	0.4352	2	44.313	44.086	43.557
J073542.51+652731.9	124	1	0.3380	1	44.248	43.948	43.927
J073725.60+654302.5	130	1	0.2660	2	43.8105	43.537	42.794
J123615.87+131524.9	131	0	0.6250	2	45.208	45.143	-
J123602.90+131826.2	133	1	0.34400	2	44.1192	43.835	-
J123620.31+130900.0	135	1	0.264	1	44.004	43.743	-
J123710.13+130137.0	136	1	0.1990	2	43.735	43.427	-
J124223.16+331323.7	137	1	-	-	-	-	-
J124236.07+331057.5	138	1	1.7280	1	45.840	45.872	44.345
J124312.15+332136.7	139	0	0.5270	2	44.494	44.385	-
J123302.45+000018.0	143	1	0.0840	2	43.708	43.430	40.298
J123322.15+000818.3	144	1	0.4420	2	44.245	43.683	42.856
J135220.58+635624.4	157	1	0.3670	2	44.118	43.747	43.006
J130738.09+291626.4	167	1	1.5091	1	45.736	45.656	44.668
J130808.51+293449.0	169	1	1.1800	1	45.389	45.207	44.258
J080646.38+153012.9	173	1	0.0920	2	42.762	42.469	40.496
J211525.48+055918.4	177	1	0.6110	2	44.699	43.949	43.568
J211516.57+060840.7	178	1	0.4010	1	44.742	44.498	43.972

WISE ID	Sample ID	Confirmed	z	Class	$L_{6\mu m}$ / erg s^{-1}	$L_{6\mu m_{AGN}}$ / erg s^{-1}	L_X / erg s^{-1}
J103336.30+573106.7	182	1	0.2955	2	43.988	43.717	43.563
J103321.11+573213.9	183	1	1.2554	1	45.564	45.312	44.570
J103411.21+575528.2	184	1	0.2030	2	43.562	43.175	41.476
J122211.33+143858.3	188	1	1.5380	1	45.529	45.543	-
J115738.35+435308.9	189	1	1.2080	1	45.688	45.554	43.791
J115835.10+434841.8	191	1	1.2400	2	45.524	45.455	43.738
J115754.96+434752.8	192	1	0.0810	2	43.0625	42.815	42.655
J115757.21+440541.6	194	0	-	-	-	-	-
J123123.16+105632.9	199	0	0.9460	2	45.116	45.026	-
J123046.60+111141.6	200	0	0.5680	2	45.001	44.924	-
J124525.12+672442.1	201	1	0.2320	2	43.912	43.596	42.655
J124615.77+673032.7	205	1	1.7656	1	46.027	45.968	45.172
J124728.49+671724.9	206	1	1.2219	1	45.441	45.295	44.526
J124756.14+671112.8	209	1	-	-	-	-	-
J102313.27+195651.9	212	1	1.0849	1	45.309	44.835	44.538
J102318.66+194835.6	213	1	1.7658	1	45.968	45.944	44.683
J102408.03+194856.2	214	1	0.8220	2	44.881	44.517	43.709
J102315.52+195850.6	215	1	0.4670	2	44.291	43.654	43.325
J102255.18+195554.4	216	1	0.3705	2	44.435	44.194	43.904
J121952.30+472058.5	218	1	0.6535	1	44.789	44.132	44.435
J121729.41+471424.8	221	1	1.0408	1	45.239	44.827	44.077
J121839.40+470627.6	226	1	0.0939	2	43.855	43.718	43.140
J131134.91+231817.0	234	1	1.5330	1	45.896	45.864	44.605
J131213.57+231958.6	237	1	1.5158	1	46.056	45.998	45.033
J131129.93+233158.3	238	1	0.4837	2	44.570	43.956	43.965
J131237.44+232906.5	240	0	0.6280	2	44.869	44.754	-
J123627.57+263151.2	244	1	1.8338	1	45.982	45.940	44.698
J123604.01+264135.9	245	1	0.2088	1	44.590	44.312	43.645
J123629.68+263650.2	246	1	0.6350	2	44.600	44.461	43.179
J215124.17-053059.8	248	1	0.4511	2	44.283	44.260	43.179

Table 5: Summary of the properties for the WISE full sample and the 5 AGN without redshift. Column 1: sample identifier of the AGN; column 2: redshift of the AGN; column 3: confirmation of the AGN nature of the object, 1 if it has been confirmed or 0 if not; column 4: classification of the AGN, 1 if it is a type 1 AGN and 2 if it is a type 2 AGN; column 5: observed mid-infrared luminosity in logarithmic units, see Section 2.3 for a details; column 6: AGN mid-infrared luminosity in logarithmic units, see Section 2.4 for details; column 7: AGN intrinsic X-ray luminosity in logarithmic units. For AGN 6, 143 and 173 we indicate their observed X-ray luminosity as they have low-quality spectra (see Section 2.3 for details). Shaded AGN belong to the CT candidates sample.